PONTIFICIA
UNIVERSIDAD
CATÓLICA
DE CHILE

FACULTAD DE FÍSICA
INSTITUTO DE ASTROFÍSICA

Host galaxies of local hard X-ray selected AGN

BY

GORAN DOLL CARRIEL

Thesis submitted to the Faculty of
Physics of Pontificia Universidad Católica de Chile (PUC),
as the requirement to qualify for the academic Master's degree in Astrophysics.

Professor Advisor	:	Dr. Franz Bauer (PUC Chile)
Co-Advisor	:	Dr. Giuseppe D'Ago (PUC Chile)
Evaluation Committee	:	Thomas Puzia (PUC Chile)
		Roberto Assef (Universidad Diego Portales)

January, 2022
Santiago, Chile
©2022 — Goran Eliot Doll Carriel

©2022 — Goran Eliot Doll Carriel

Se autoriza la reproducción total o parcial, con fines académicos, por cualquier medio o procedimiento, incluyendo la cita bibliográfica del documento.

Acknowledgments (in Spanish)

Me gustaría dedicar el siguiente trabajo a varias personas que han contribuido enormemente al desarrollo de este proyecto a lo largo de más de dos años. Sin orden en particular:

A mi Profesor guía Franz Bauer. Por su extrema paciencia, simpatía e inteligencia, le estoy muy agradecido. A él le debo mucho de este trabajo.

A mis viejos y nuevos profesores y guías, con especial mención al Dr. Sebastien Guillot y el Prof. Andreas Reisenegger, que me embarcaron en la aventura de la investigación.

A mis compañeros y compañeras de postgrado y a mi grupo de investigación, que fueron (y siguen siendo) fuente de motivación y de retroalimentación durante todo el desarrollo de mi Magíster. A mis amigos del pasillo y sobretodo a la Cafetería 116: Carolina, Felipe, Diego y Gonzalo: les debo mucho más de lo que creen. Me gustaría agradecer especialmente a Giuseppe, a quién le debo mucho del conocimiento técnico requerido en esta investigación. Gracias también al equipo de BASS, pues sin su trabajo el mío probablemente no habría comenzado.

Finalmente, a mi familia, en especial a mis padres y hermanas. Aunque no lo suela decir en palabras, les estoy agradecido de por vida por su apoyo incondicional.

Contents

List of Figures

Draft version February 7, 2022
Typeset using LaTeX default style in AASTeX63

Abstract

We investigate the evolutionary state of galaxies hosting active galactic nuclei (AGN) for a sample of 138 hard X-ray selected AGN from the BAT AGN Spectroscopic Survey (BASS) catalog and which have high-resolution (R $\sim$ 5000), VLT/X-SHOOTER 0.3–1 μm spectroscopy. We perform a stellar population synthesis analysis via pPXF fitting of the stellar continuum, as well as fit specific emission and absorption features (e.g., Lick indices, line ratios), to estimate AGN/star formation contributions, dust obscuration, stellar age, metallicity and star formation histories. Additionally, we perform morphological classification on our sample to study possible correlations to said evolutionary state. We compare our results to AGN X-ray properties and infrared (IR) derived SFRs to estimate the potential for AGN feedback. Using several cuts and selection criteria, we construct a comparison sample from SDSS DR7 data in the MPA-JHU catalog to place our AGN sample in the context with overall galaxy evolution. The X-SHOOTER spectra primarily probe the central regions of the AGN hosts, which tend to be dominated by old ($>$ 10 Gyr) stellar populations. However, we find our sample primarily composed of main-sequence spirals (46%), followed by green valley spirals (14%) and green valley ellipticals (14%), with almost no galaxies present in the red sequence according to our definition. Our spectral modeling suggests that most elliptical and blue spiral hosts of AGN experienced strong episodes of star formation at intermediate ages ($\sim$ 1–6 Gyr), which strongly correlate with their apparent morphological features (tails, remnant features). In contrast, most red spirals seem to follow a completely secular evolution. Comparison of IR and optically derived SFRs for 57 AGN in the sample implies copious obscured star formation; this appears to push otherwise optically passive elliptical hosts into the green valley or main sequence. As for the effect of AGN feedback, we only find very mild correlations between the AGN and the host bulge properties, thereby implying weak links between the current AGN event and their intermediate-age populations.

Keywords: AGN — stellar populations — catalogs — surveys

1. INTRODUCTION

1.1. *Overview*

The rapid progress of wide-area optical surveys over the past several decades has led to a clear and striking empirical picture of massive galaxies. For instance, we observe a distinct bimodality of galaxies in the color-magnitude diagram, characterized by a narrow band of red galaxies ('red sequence') and a more diffuse one spanning a more extensive range of bluer colours ('blue cloud') (Strateva et al. 2001, Bell et al. 2003). Subsequent works found a similar, more physically oriented separation when analyzing (specific) star formation rates and stellar masses, which defined a "main sequence" of star-forming galaxies, synonymous with the blue cloud, and passively aging (so-called "red and dead") galaxies with much weaker star formation rates associated with the red sequence (see, e.g, Peng et al. 2010).

The spread in the color-magnitude diagram highlighted two physically distinct types of galaxies, which was further supported by spectral information, revealing old stellar populations dominating the stellar continuum of red sequence galaxies. In contrast, the continuum of blue cloud galaxies tends to show stronger signatures of young stars. Morphological studies revealed that the red sequence is dominated by elliptical/S0 galaxies, whereas the blue cloud is composed of primarily spiral and irregular ones. Any explanation of this picture requires an evolutionary transformation to explain why the morphological and kinematic features (e.g., surface brightness profiles and stellar motions) as well as the stellar histories of massive red galaxies differ from the case of main sequence galaxies.

Ever since the Sloan Digitized Sky Survey (SDSS) so clearly and sharply demonstrated the existence of this bimodality, the scientific community began to pay attention to the gap region between the red sequence and the blue cloud, commonly called the 'green valley'. This relatively sparse region has been a focus of debate, as it might reveal insights into the transitions from one distribution to the other and thus help in understanding why star formation may cease ('quenching') and/or reignite in some galaxies. In particular, the scarcity of galaxies in this region was argued to imply a rapid transition of some main-sequence galaxies to the quenched ones via one or more physical mechanisms that halt star formation in blue galaxies (see, however, e.g., Schawinski et al. 2014 for a more modern hypothesis).

Another observational evidence is the number densities of galaxies and their morphologies. The number densities are closely related to the luminosity function of galaxies (LF) and their evolution, and modern cosmological simulations should predict them correctly. However, the ends of the LFs have been shown to have two distinct properties that are hard to predict for a lambda CDM model: an exponential cut-off at the luminous end and a flat faint-end (Benson et al. 2003). As a result, supernova feedback is commonly invoked with some success to solve and correctly fit the fainter end for the less massive dwarf galaxies. However, it is insufficient to suppress star formation for massive galaxies, and a second quenching mechanism is needed to heat or move the gas. Although hard to probe, Active Galactic Nuclei (AGN) feedback has been a popular solution (e.g., Bower et al. 2006; Dubois et al. 2016 for a modern simulation).

There are several reasons why AGN have been consistently proposed as a feedback source (Fabian 2012). AGN hosts have been shown to preferentially lie in the green valley (within a mild shift in magnitude; Schawinski et al. 2009). Moreover, due to their extremely high efficiency in converting infalling gas to energy, accreting supermassive holes (SMBHs) are prime candidates to affect galaxies' gas content and, consequently, their star formation. This idea is supported by strong correlations between the mass of SMBHs and their host galaxy properties (see, e.g. Gültekin et al. 2009), which suggests a co-evolution of SMBHs with their host galaxies.

Despite the above, the role of AGN feedback in galaxy evolution has not been easy to probe. AGN produce strong spectral features that can often be seen throughout all bands and thus complicate spectral analyses of host properties. In the optical band, AGN can photoionize the gas, so we cannot directly rely on features such as Hα for deriving accurate SFRs. In the infrared (IR) band, the AGN contribution can be significant and must be decoupled from dust emission due to star formation. Moreover, the ages of the stellar population heating the dust are very difficult to constrain.

On the other hand, a variety of circumstances complicate the selection of AGN in an unbiased manner. For instance, optical selection techniques can miss weak AGN with high levels of ionization from other sources (e.g., starbursts). Additionally, high levels of obscuration and dust extinction in Type-II AGN limit their detectability in the optical band. Due to these biases (see e.g., Mushotzky 2004), hard X-ray selection techniques are considered the most robust method to obtain a relatively unbiased census of strongly accreting SMBHs. More specifically, the ultra-hard X-ray (14—195 keV) Swift–BAT all-sky survey is considered to be provide the most sensitive census of AGN in the local universe. The most recently published catalog is the 105-month depth one (Oh et al. 2018), which contains 1016 AGN among 1632 total sources. As the 14—195 keV band suffers from much less contamination than the optical and IR-bands, it provides an unprecedented level of completeness for the characterization of (local) AGN properties and evolution; specifically, it only remains insensitive to very high Compton thick AGN ($N_H > 10^{25}\text{cm}^{-2}$) and very low luminosity AGN.

The BAT AGN spectroscopic survey (BASS; Koss et al. 2017) provides optical/NIR spectroscopy and multi-wavelength data for nearly all of the Swift–BAT all-sky survey AGN, and thus provides an excellent resource to study the hosts of AGN as a whole. The size and quality of this sample make it the best to date for a confident, high spectral resolution spectroscopic study of a nearly-unbiased AGN selection. Throughout this work, we attempt to take advantage of this privileged selection to take a first step in the global, unbiased and robust characterization of the properties of AGN hosts in the local universe.

In this work, we utilize stellar population synthesis to study population properties in the central few arcseconds for a sample of 138 local galaxies associated with BASS AGN, using recent, high-resolution optical and near-UV spectra. This technique allows us to simultaneously fit a set of templates to our spectra via χ^2 minimization. In this way, we can retrieve weights that describe the final fitted model as a linear combination of our templates. We also fit ionized gas emission lines and compute Lick indices to further characterize the evolutionary state of our sample. In particular, we are interested in comparing different star formation tracers to understand their differences, particularly as they pertain to any hidden star formation that may not be sampled by our stellar population modeling. In the intermediate sections of this thesis (particularly Section 4.2), in order to study AGN feedback, we attempt to correlate different bins and percentiles in each SFH distribution to various AGN properties from Koss et al. 2017. We also perform a morphological classification of the sources to assess their structure and past history. In our later sections (most of Sections 4 through 5), we attempt to characterize the evolutionary state of BASS AGN hosts. To this end, we utilize stellar population synthesis results to derive individual SFHs for most of our sample. From there we compute medians across the sample to characterize the typical SFHs of the various groups (sorted by morphological features) of galaxies within our schemes. Finally, we use IR SFR measurements coupled with our morphologic classification and SFHs to determine the evolutionary state of the sources within our sample. With some caveats, this analysis provides a preliminary step for the complete characterization of AGN hosts.

The structure of the thesis is as follows: In the remaining part of Section 1, we give a brief introduction to stellar population models and a basic background of AGN and their role in galaxy evolution. In Section 2, we describe our data set and observing setup. In Section 3, we describe our method and pipeline for our stellar population fitting. Finally, Sections 4 and 5 present our results and conclusions, respectively, covering comparisons of Hα derived star formation rates to infrared derived rates and their interpretation. Throughout this work, we use the cosmological parameters derived by the nine-year Wilkinson Microwave Anisotropy Probe (WMAP) mission, further detailed in Hinshaw et al. (2013).

1.2. *Stellar population models*

A fundamental component of galaxies are their stars. A proper study and modelling of galaxy spectra should shed light into what kind of stars shine the light we see, which would allow us to recover important parameters such as the star formation history, metal composition and total stellar mass. The simplest model one can use is the so-called *Simple stellar population (SSP)* model. This consists in the characterization of the stellar mass as the result of a group of stars which have a common origin (they are coeval) and thus, they share similar chemical and orbital properties. Although this can only be applied to stellar clusters in principle, the stellar component of a galaxy can be seen as the linear sum of several SSPs. Naturally, such a model needs either a theoretical or empirical basis to be sustained. The first model ingredient to characterize a population is the Initial Mass Function (IMF): the group of stars that describe the stellar population should follow a certain number distribution in mass at birth. This distribution may not be the same for every population, and is indeed hard to measure (Salpeter 1955). A second ingredient is a prescription for how the stellar mass of a certain age and metallicity range is converted to light, which can allow for the building of isochrone libraries, when combined with a choice of the IMF. These libraries describe the position in the luminosity-surface temperature plane of several groups of stars of different ages and metallicities depending on their state of evolution (this also includes mass loss histories in the red giant branch and asymptotic giant branch). Finally, one also needs a *spectral library* of a certain resolution, either empirical or theoretical, that contain actual spectral information needed to ultimately perform a fit to the data. The selection of a particular stellar library will largely depend on the specific study case, and depending on the wavelength coverage, spectral resolution, age/metallicity coverage, and the inclusion of fundamental processes such as mass loss mechanisms.

In practice, an extra ingredient is a software with a particular mathematical method that can properly fit the data using the spectral libraries, despite the large amount of degeneracy that this analysis usually includes. In this study, we choose the Penalized Pixel-Fitting package (pPXF; Cappellari & Emsellem 2004, and later upgraded in Cappellari 2017), which uses a technique called *regularization*. This technique allows to give preference to the smoothest solutions among many that retrieve similar fit statistics, avoiding unrealistic results. In addition to this technique, pPXF allows for the inclusion of polynomials and a reddening curve to the SSP models, useful to properly model and characterize the data and results.

As a caveat, we want to emphasize that pPXF (and any other similar tool) is given the task to retrieve solutions to both an ill-posed and an ill-conditioned problem. More specifically, the issue of retrieving age and metallicity solutions is a problem which may not have a unique solution (ill-posed) and the solution itself can be significantly affected and limited by a certain quantity (ill-conditioned), which in our case corresponds to the S/N. Moreover, the effect of dust and AGN contamination pose a further complication for any potential solution to this highly-degenerate problem. Therefore, much of our analysis carries implicit uncertainties which are extremely difficult to quantify. While not explicitly considered, we estimate that a (rough) mean error up to $\approx$0.5 dex is present in the estimation of both the age and metallicity of any stellar population. This quantity is justified to an extent by past studies (Worthey 1994) and can also be seen empirically by perturbations to pPXF input parameters (regularization strength and noise level), which can often not distinguish if a certain old and metal-poor population is, in reality, part of a different metal-rich, younger population. While this issue is not completely solved, the weight distribution of pPXF can serve as a tool to reveal the degeneracies at a certain S/N level, which are often well-constrained enough for good choices of the regularization strength.

1.3. *The global properties of galaxies*

This work aims at comparing the properties of AGN host bulges and central regions, to similar stellar population properties of all kinds of nearby galaxies within our stellar mass and redshift coverage. For this reason, we summarize three of the most relevant global properties of galaxies, evident when analyzing large catalogs:

- The bimodal distribution: Ever since the release of the Sloan Digital Sky Survey (SDSS; York et al. 2000; Gunn et al. 2006), the separation of red from blue galaxies has become very evident. Since then, much progress and efforts have been made to explain the formation and interaction between these distributions, and their relation to a similar kind of bimodality: the morphology classifications and features that are often associated with early-type galaxies from late-types. In particular, a natural explanation for the apparent strong contrasts is to consider processes such as mergers and feedback to explain the state and evolution of the gas reservoir in galaxies, and ultimately their depletion and active transformation into stars (or lack thereof).

- The overall star formation history of the universe: Various thoughtful analyses of the star formation rates of nearby and high-z galaxies show a rise and decay of the global star formation rate of the universe with a peak at around $z \sim 2$ (see e.g, Madau et al. 1998 and Madau & Dickinson 2014). This suggests a global scenario that has to include significant star formation at early epochs, and one or more methods for the quenching of star formation.

- The role of morphology and mergers: The above processes are, most likely, different for each type of galaxy (red and blue; or early-type and late-type) and thus may have different timescales. Mergers have been proposed as a means of rapidly quenching star formation (Baldry et al. 2004), in conjunction with AGN feedback processes. More recently, Schawinski et al. (2014) developed a model where early-type and late-type galaxies are analyzed and characterized separately. In this picture, late-type galaxies quench slowly due to the shut-off of gas supply, whereas early-type galaxies must have passed through a violent mechanism of gas removal and stellar angular momentum randomization.

1.4. *The role of the AGN*

In the search for processes that are strong enough to alter the state of the gas in galaxies, AGN have been a popular case of study. This is not surprising, considering the high efficiency in the conversion of gravitational energy to light, revealed by the extremely high X-ray luminosities of AGNs, which can reach $L_X \sim 10^{48}$erg s^{-1}. Moreover, the position of AGN in the color-magnitude diagram (see, e.g Schawinski et al. 2009) reveal a predominance of green colors, which support the case that AGN could be transitional sources between blue and red distributions of galaxies. Lastly, the co-evolution of the SMBHs with their host bulges (Gültekin et al. 2009) is an interesting link between host and nuclear properties, although similar to the other points presented here, it does not probe the AGN as a cause for feedback nor for the transition of galaxies through the green valley. It is also important to note here that the inherent contamination of the AGN spectra to the optical and ultraviolet light might bias the measured colors of AGN hosts. This is especially true for Type-I AGN. Type-I AGN, according to the orientation-based Unified Model for AGN, are sources for which the broad line region of the AGN (BLR) is not obscured by its fiducial torus gas (whereas Type-II AGN are obscured) because we are viewing the opening of the torus face-on. The strong continuum from the accretion disk and broad line emission from the BLR can easily contaminate the stellar continuum and become a major problem. For this reason, we exclude most sources in this work that are AGN-dominated in the optical band and henceforth restrict most of our interpretations and conclusions to the spectra of the central regions of Type-II AGN. Regarding the potential bias of this approach, orientation-based AGN unification would not predict any significant bias between the host properties of both AGN types, since their classification arises purely from our random line-of-sight view with respect to their torus position. Overall, most studies seem to agree with this picture with some caveats (see e.g, Zou et al. 2019, Koutoulidis et al. 2021).

2. DATA AND OBSERVING SETUP

2.1. *Spectral data*

Our principal sample is comprised of observations carried out with the multi-wavelength echelle spectrograph X-SHOOTER at the Very Large Telescope of Paranal Observatory in Chile (VLT). Our initial, 165 source X-SHOOTER sample primarily results from a series of targeted filler programs carried out through several semesters (098.A-0635,099.A-0403, 0101.A-0765, 0102.A-0433, and 0103.A-0521), mostly aimed towards local observable, type-II AGN located in the southern hemisphere. We use observations taken through July 26, 2019. Due to the limited availability and wavelength range of the high-resolution templates, we only focus on the information from the optical and UV arms of X-SHOOTER, covering a spectral range of 3000–10000 Å. The median seeing for this data is 1.0” with a standard deviation of 0.4”, and the spectral quality resulted in signal-to-noise ratios (SNRs) varying from $\sim$0.7 to $\sim$210, with a median of $\sim$13 per spectral resolution element. The optical and UV arms have an overall lowest spectral resolution of 3.3 Å FWHM, which we later fix at this value (see 3.1). For 26 sources, we are unable to recover complete wavelength coverage due to poor calibration of the optical arm, which ultimately translates into an inability to measure Lick $H\delta_A$ indices (see 3.10). However, analysis of the near-UV arm alone allows us to place reasonable constraints on the stellar population, and thus we decide to keep and include these spectra in our science sample.

The X-SHOOTER sample is based on the 105-month catalog, and comprises a substantial subset of the new spectra obtained for BASS DR2. We note that previous spectroscopy for BASS DR1 was primarily of an archival nature and based on the 70-month Swift-BAT all-sky catalog, while the new X-SHOOTER spectra largely target new fainter AGN that were previously not incorporated and/or had poor SNRs in previous spectra. As such, they inherit some bias against very high luminosity AGN (log $L_{bol,X} > 46$ erg/s), and therefore primarily against strongly beamed AGN in high-mass galaxies, which are not very reliable or relevant for our current study in any case. Ultimately, this new sample and its addition to BASS allow for a more complete AGN selection in luminosity and spatial coverage. We restrict ourselves mainly to X-SHOOTER data because it comprises a previously unstudied set of spectra regarding stellar population analysis. More specifically, the XSHOOTER sample is more sensitive to fainter, narrow-line AGN compared to earlier spectra, and thus provides a more reliable way to measure a clean non-AGN-dominated star formation continuum. Figures 4, 5 and 6 highlight the parameter-space coverage of the X-SHOOTER sample compared to the overall BASS DR2. Moreover, the XSHOOTER sample provides uniform, broad optical wavelength coverage and the highest spectral resolution amongst the BASS DR2 sample.

Compared to modern optically-selected samples of AGN, the X-ray selection preferentially finds high luminosity AGN, including large numbers of heavily obscured AGN. As an example, recent works using the MaNGA sample (Bundy et al. 2015) tend to find more common but comparatively lower bolometric luminosity AGN. This is because the MaNGA galaxy selection randomly samples the galaxy population across a broad range of parameters, while powerful AGN tend to be rare and generally reside in massive hosts, These MaNGA studies use BPT diagnostics and Hα equivalent widths as selection criteria in small apertures (Rembold et al. 2017; Sánchez et al. 2018) or spatially resolved regions (Wylezalek et al. 2020), allowing to dig out faint AGN among galaxy host contamination. The MAGNA AGN typically have [OIII] luminosities of $L_{[OIII]} \sim 10^{40}$ erg s^{-1}, which translates to bolometric AGN luminosities of $L_{bol} \sim 10^{43}$ erg s^{-1} (Wylezalek et al. 2020), which is comparable to the lowest ∼5% of the BASS DR2 sample. In contrast to the above, a small portion of our sample would be rejected as AGN based on an optical BPT classification, due to a mix of both AGN and star formation photoionization (see 3.7). Thus, our sample traces a different set of sources, among which some may present various sources of photoionization in their central regions.

To calibrate our measurements to our comparison sample, we also analyze 15 Sloan Digital Sky Survey (SDSS; York et al. 2000; Gunn et al. 2006) DR12 legacy observations of Swift-BAT sources. From the 118 SDSS spectra available from BASS DR2 (Oh et al., submitted), we select a fraction of Type II hosts (with no major signs of AGN contamination) which are suitable for our pipeline (recovering high SNRs and SRRs as per 3.2). SDSS spectra cover a slightly narrower wavelength range of 3800–9200Å and have a resolution of 2.76Å. After adding SDSS spectra, our initial sample before any filtering totals 180.

In terms of extraction aperture sizes, X-SHOOTER sources are assessed with a 1.6” slit × 4” width and SDSS sources with a 3” fibre diameter. X-SHOOTER data were reduced using the standard pipeline for nodding observations (`xsh_scired_slit_nod`) in the ESO reflex software (Freudling et al. 2013). The basic steps include bias correction, wavelength calibration, frame stacking, and sky subtraction. This later procedure is based on the double-pass nodding scheme used in IR observations: for our sample, a nodding box of 5” and an extraction region of 4” along the slit are used. We refer to den Brok et al. 2021 (submitted) for more details about the reduction steps.

Note that we only plot a fraction of our sample (115/180) in Fig. 4. This corresponds to all sources in our sample that have passed our rejection pipeline (see subsection 3.2) and have both BH mass and X-ray luminosity measurements (see Oh et al., submitted).

2.2. *Images*

In addition to the spectral information, we retrieve color image cutouts (with an *asinh* stretch) for all available sources in our sample from, in order of preference, the DESI Legacy Imaging Survey DR9 (*grz* Dey et al. 2019), SDSS DR15 (*gri* Aguado et al. 2019), PanSTARRS-1 DR2 (*grz* Chambers et al. 2016), STScI DSS (blue, red and NIR bands; Space Telescope Science Institute Digitized Sky Survey; Lasker et al. 1996), or unWISE (*grz* Lang 2014). We classify 129 galaxies morphologically (see §3.11 for details on the classification scheme), including all sources with clean cutouts (no artifacts) in critical images. Of these 129 galaxies, 95 present high spatial resolution cutouts, meaning they have at least a Legacy, PanSTARRS, or SDSS cutout. The rest of galaxies present only low-resolution cutouts. Example cutouts are shown in Figs. 1 and 2.

2.3. *Multiwavelength measurements*

Throughout this work, we incorporate a variety of estimated physical properties which have been measured by the BASS collaboration for 115 of the 138 eventual sources used for spectral fitting (see Sec 3.2). Namely, this includes 81 stellar masses from Secrest (2022, in preparation), 115 black hole masses from Koss et al. (2017), 115 X-ray luminosity

(a) (b) (c) (d)

Figure 1: Color image cutout example (BAT-ID 669) for the (a) DESI Legacy Imaging Survey DR9 (*grz*), (b) SDSS (*gri*), (c) PanSTARRS (*grz*), and (d) STScI DSS2 (Blue/Red/NIR filters). The primary classification is *Spiral*, with a *Companion* as its secondary one. As such, we flag this galaxy as having a dynamical morphological feature.

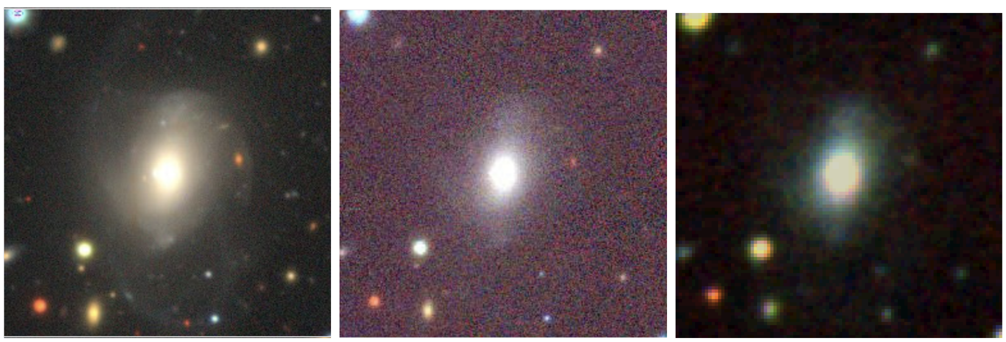

(a) (b) (c)

Figure 2: Color image cutout example (BAT-ID 135) for (a) DESI Legacy Imaging Survey DR9 (*grz*), (b) PanSTARRS (*grz*), and (c) STScI DSS2 (Blue/Red/NIR filters). The primary classification is *Elliptical*, while only the DESI Legacy cutout enables us to add a secondary, more specific morphological classification (in this case, merger remnant).

and 83 column density ($N_{\rm H}$) estimates from Ricci et al. (2017) and 112 and 29 infrared star formation rates from Ichikawa et al. (2019) and Shimizu et al. (2017), respectively. We refer to these works for their respective derivation. The principal reason why these numbers are lower than our full sample of 180 sources and vary is because they are based on the 70-month Swift-BAT all-sky catalog, as well as the availability of key multiwavelength observations and our data filtering.

3. METHODS

3.1. *Spectral fitting procedure*

As an initial preparation, and to take advantage of our data, we splice the VIS and UVB arm spectra together to enable a joint fit of the full wavelength range. To recover the ages and metallicities of the stellar populations, we begin by fitting the stellar continuum of all the 180 spectra from our sample. The Penalized Pixel-Fitting package (pPXF; Cappellari & Emsellem 2004) uses single stellar population synthesis (SSP) models and allows for the masking of gas emission lines and low-SN regions. Moreover, it allows for the fitting of either a reddening curve or multiplicative and additive polynomials, and thus is ideal for our purposes. Our model consists of 216 stellar templates from E-MILES

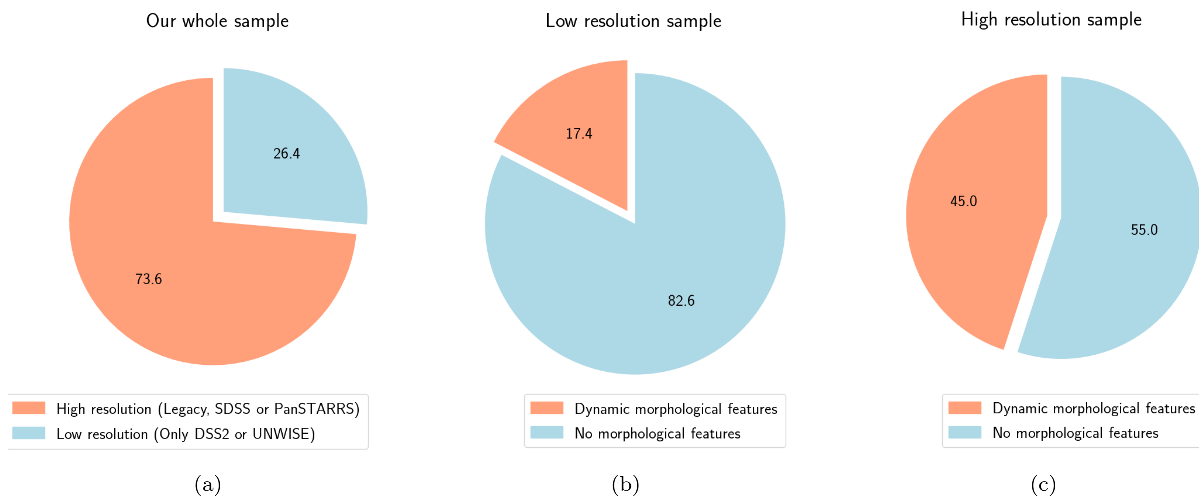

Figure 3: Pie diagrams of our sample indicating the relative fraction with high spatial resolution imaging (either SDSS, Legacy or PanSTARRS) among 129 morphologically classified galaxies (a), as well as the relative fractions of sources identified to have dynamical morphological features in the low-resolution (b) and high-resolution (c) imaging. We see a notable increase in the relative number of dynamical morphological features going from (b) to (c).

BaSTI (a Bag of Stellar Tracks and Isochrones, Percival et al. 2009) that assume a unimodal Initial Mass Function (IMF) with a logarithmic constant of 1.3 and span an age range of 0.03–13.5 Gyr (the upper bound is adjusted based on redshift), metallicities covering $-2.27 < Z < +0.4$, and a wavelength range that fully covers our data and thus is useful to fully utilise both optical and UV arms of X-SHOOTER. In this study, we are also interested in recovering the stellar-derived extinction along the line of sight ($A_{v,stars}$) for our sources, and thus add an extinction law based on Calzetti et al. (2000) to recover this parameter. The use of multiplicative and additive polynomials is frequent in the literature as it helps to account for spectral calibration issues and template mismatching. In this work, however, we decide to avoid them, as they are degenerate with our reddening model.

For the data, an additional step is necessary before the actual fitting: because the templates have a fixed FWHM per-pixel resolution of 2.51 Å, which is lower than the X-SHOOTER spectral resolution over much of the UV+optical range, we decide to bin the resolution of all the X-SHOOTER spectra to a constant FWHM of 3.3 Å, which is the lowest resolution present in the data. As the expected velocity dispersions of the host galaxies in our sample are generally higher than the resolution of the instrument, we do not expect this to significantly affect our analysis.

Using pPXF, we run a first fitting iteration utilizing the standard, built-in masking technique present in pPXF to quantify the strong residuals made by emission lines and sky features. This technique consists of masking spectral windows (widths defined by the user) centered in rest-frame line wavelengths catalogued by the software. Due to its simplicity, this method alone fails to mask all of the emission lines present in every spectrum and suffers problems for low S/N spectra and sky-line dominated regions. Nevertheless, it serves as a first step for our final masks. Depending on the strengths of the fit residuals in this previous iteration, we set a masking threshold for every spectrum as a single value that determines the number of pixels to be later masked in a second iteration via a simple sigma-clipping technique. To further optimize S/N, we also cut all of the spectra at rest-frame 8662 Å (i.e., 300 Å longward of the

CaII triplet). Although most of our sources have been corrected for telluric absorption, some sources remain affected by these features, especially in the optical X-SHOOTER's arm data. We find that removing this range significantly improves the quality of the data, without degrading estimates of higher-order galaxy properties.

3.2. *Data filtering*

The fit quality of the data is assessed through visual inspection, and further quantified using signal-to-residual ratios (SRRs) and SNRs. For instance, we remove low S/N or poorly fit spectra from our sample as follows: we exclude S/N < 5 or strongly AGN-dominated spectra (mostly, Blazars and Seyfert 1 (1.0–1.9) galaxies with weak stellar continua that our pipeline fails to properly fit), which have significantly low values of SRR for their SNR. We plot the SNR and SRR of our rejected and accepted sources in Fig. 7. We note that a large portion of our rejected sources lie significantly outside of the dominant linear relation (with a mean $\chi^2 \sim 5$). For others, they lie within 1σ of the relation, but possess strong Type-I AGN emission features that prohibit our stellar population analysis from retrieving reliable results. In a few cases, the spectra were either contaminated from a foreground star, or had a mismatch between the redshift from their absorption features compared to their emission features. We can sometimes retrieve a reasonable fit, but it is less accurate and moreover is unclear how to interpret, and therefore we avoid including them in our final sample. In practice, this data filtering removes 42 sources, leaving 138 X-SHOOTER+SDSS sources available for science purposes. We again note that our filtering introduces a mild bias against high-z, beamed X-ray selected AGN.

3.3. *Error estimation*

In addition to age-metallicity degeneracy effects, a natural source of uncertainty in our results comes from the selection of our pixel mask. This is exacerbated when there is degeneracy in our data and modeling, and/or when applying mass weighting to assess the contribution of older stellar populations, which are often hard to quantify in spectra that are naturally dominated by light from younger stars. To quantify variations in the weights and to estimate uncertainties, we adopt a Monte-Carlo technique to assess mass-weighted median ages and metallicities derived from our pPXF fitting procedure. In particular, we randomly mask 10% of the unmasked pixels in the spectra and refit the modified spectra. Due to computational limitations, we perform 100 iterations for each source, from which we construct distributions to estimate uncertainties.

3.4. *SFH extraction and PSB identification*

To quantify the presence of young or intermediate stellar populations in the nuclei of AGN host galaxies, we calculate age percentiles based on their binned star formation histories (SFHs); for instance, the age at which the last 20% of the stars were formed. Moreover, we try to identify special galaxy populations such as PSBs and/or starbursts, and quantify the relative strengths of the star formation episodes. To this end, we use the mass weights we get as the result of the stellar population fitting from pPXF, initially collapsing and summing them over all metallicities. Then, we divide each normalized weight by their corresponding age interval. Lastly, we renormalize the sum of the resulting mass-weighted SFH distribution to unity for later analysis and manipulations. Due the age-metallicity degeneracy

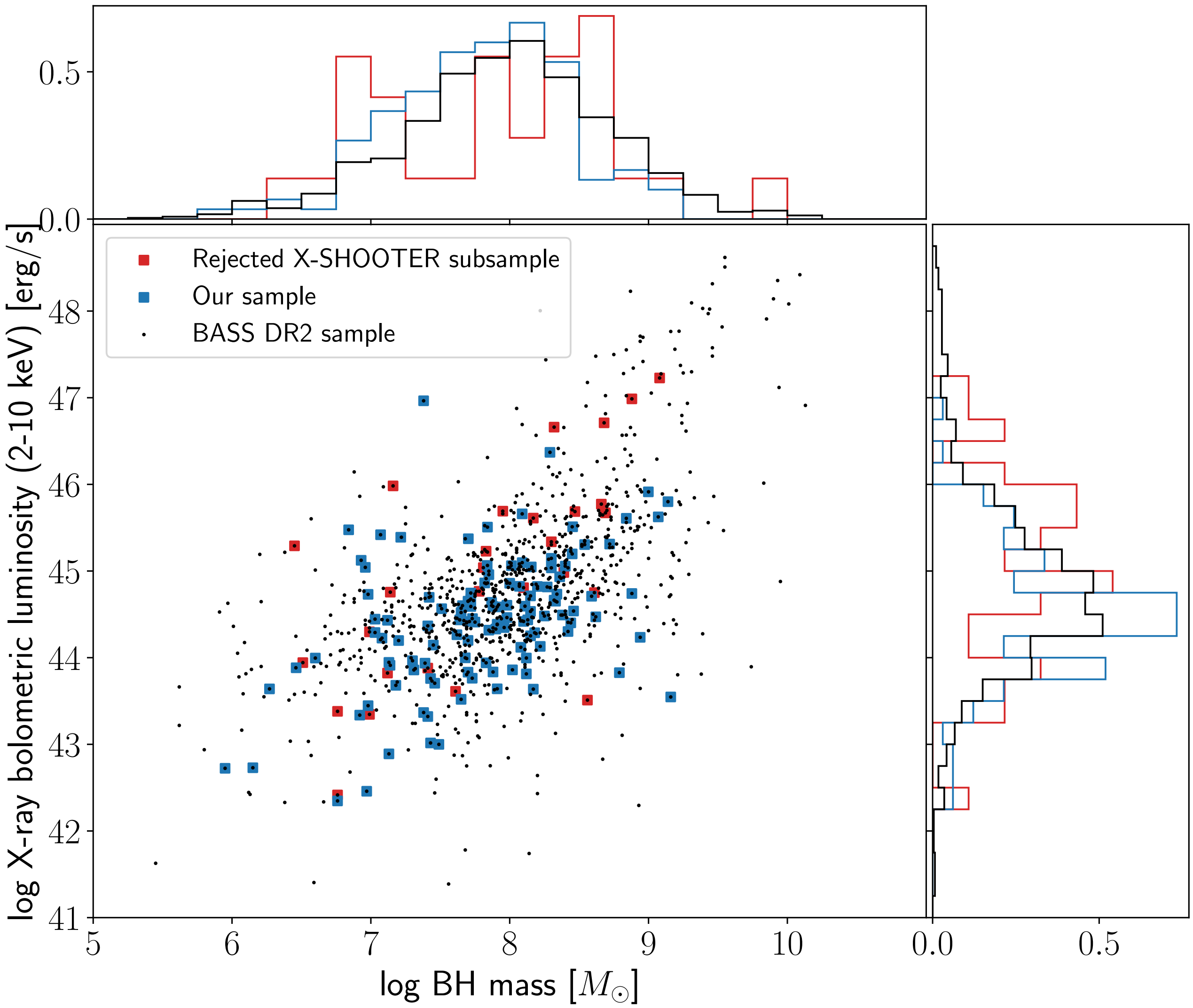

Figure 4: BH mass versus X-ray luminosity (2–10 keV) based on the 105-month Swift-BAT catalog. In *blue*, we plot 115 AGN in the X-SHOOTER+SDSS sample, while in *red*, we plot a subset of 28 galaxies from the 42 AGN originally included in our X-SHOOTER sample that were ultimately discarded (see subsection 3.2). Blue and red squares correspond to all sources with both black hole mass and X-ray luminosity measurements. In *black* dots, we plot the parent BASS DR2 sample. Note our bias against very X-ray luminous sources ($>10^{46}$ erg s^{-1}), which generally correspond to high-z, high mass, beamed AGN (Koss et al. 2022, submitted).

problem addressed in earlier sections, there is a related uncertainty in the resulting SFH of any galaxy. Because our analysis is not very sensitive on the specific age and metallicity of individual populations (see Sec. 3.5) as we mostly focus on a very broad classification of the SFH features, we expect these errors to only mildly affect our analysis.

We extract percentiles from each SFH in our sample, and we choose the 20th percentile age as a tracer for intermediate-age populations. Along with this quantity, we also extract Hδ lick indices using the `pyphot` package, which can also be used as a similar tracer and serve as a self-consistency check. Due to the strong AGN nature of the photo-ionization, we do not use a traditional Hα cut in our selection. Instead, we classify a source as a PSB candidate if Lick H$\delta > 2$ (a slightly less conservative cut; see Goto 2007, Chen et al. 2019 for examples on previous selections)

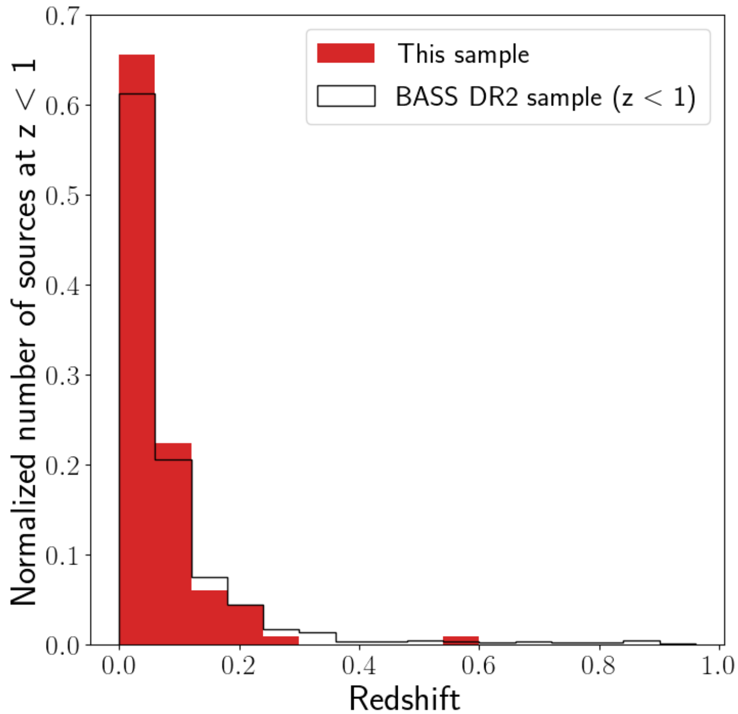

Figure 5: The redshift distribution of our X-SHOOTER sample compared to the entire BASS DR2 sample based on the 105-month Swift-BAT catalog. This only includes BASS DR2 sources with ($z < 1$) for visualization purposes. Each distribution is normalized to the unity independently.

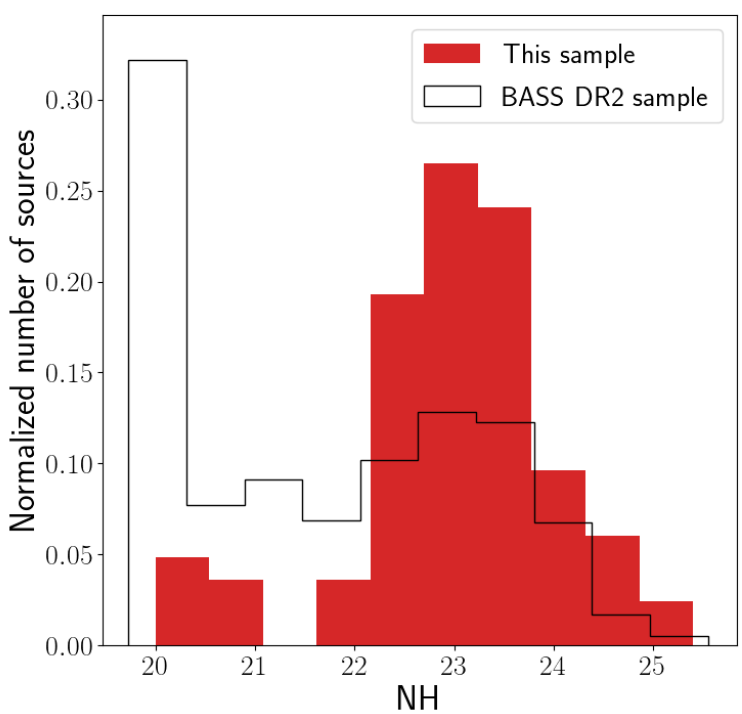

Figure 6: The $N_{\rm H}$ distribution of our X-SHOOTER sample compared to the entire BASS DR2 sample based on the 105-month Swift-BAT catalog. Each distribution is normalized to unity independently.

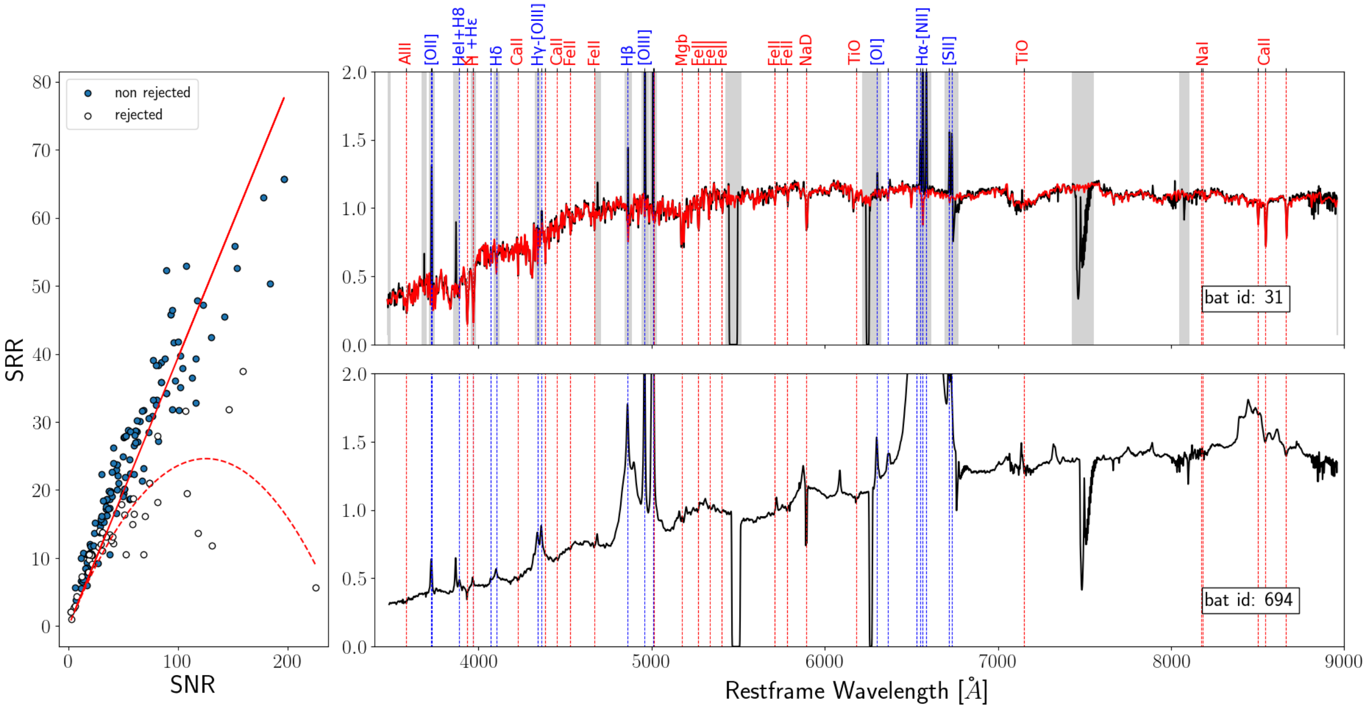

Figure 7: *Left*: SNR versus SRR for all the fitted sources in our sample (see Appendix for the details on both parameter calculations). The solid and dashed red curves are 1 and 2-degree polynomial fits to the accepted and rejected spectra, respectively. *Upper Right*: An example of an accepted source with a successful fit. The rest-frame spectrum is shown in black, and the fitted model in red. The gray regions represent our automatic mask for this case. Vertical dotted lines denote the wavelengths of common and relevant emission (blue) and absorption (red) lines. *Bottom right*: Same as above, but for a rejected source. This AGN-dominated spectrum lacks strong absorption features, and despite having a high S/N (S/N>5), it does not meet our fit quality criteria. For this reason, we do not provide a mask or model fit.

and analyze their SFH to either confirm or reject this possibility. Because the definite selection comes from the star formation histories at intermediate epochs, this slightly less conservative cut in Lick Hδ allows the criteria to stay relatively close to traditional selections, but at the same time allows for stellar population synthesis model fits across the entire spectrum wavelength range to be the deciding factor when addressing the PSB classification.

To study the possibility of star formation being impacted by SMBHs, we retrieve useful quantities from BASS collaboration studies (Koss et al. 2017), such as Eddington ratios, galaxy types, gas column measurements, and stellar masses. We look for potential correlations by comparing our quenching and current star-formation tracers to BH masses and Eddington ratios from (Koss et al. 2017). We also study our sample's stellar masses and our PSB candidates' properties against the overall selection and the larger BASS catalogue.

3.5. *The distribution of SFHs and their average*

In order to visualize the broad star formation properties of our sample, we plot individual normalized SFHs in Fig. 8. Although the median age is certainly consistent with other studies for nearby quiescent galaxies (see, e.g., Pacifici et al. 2016), we note that many galaxies have a relatively flat SFH or show the presence of a secondary peak at intermediate epochs (1–4 Gyr). This appears to occur across all stellar mass groups. The prevalence of a late-to-intermediate population in the BASS AGN sample (effectively placing them in the green valley of the color-magnitude diagram) can

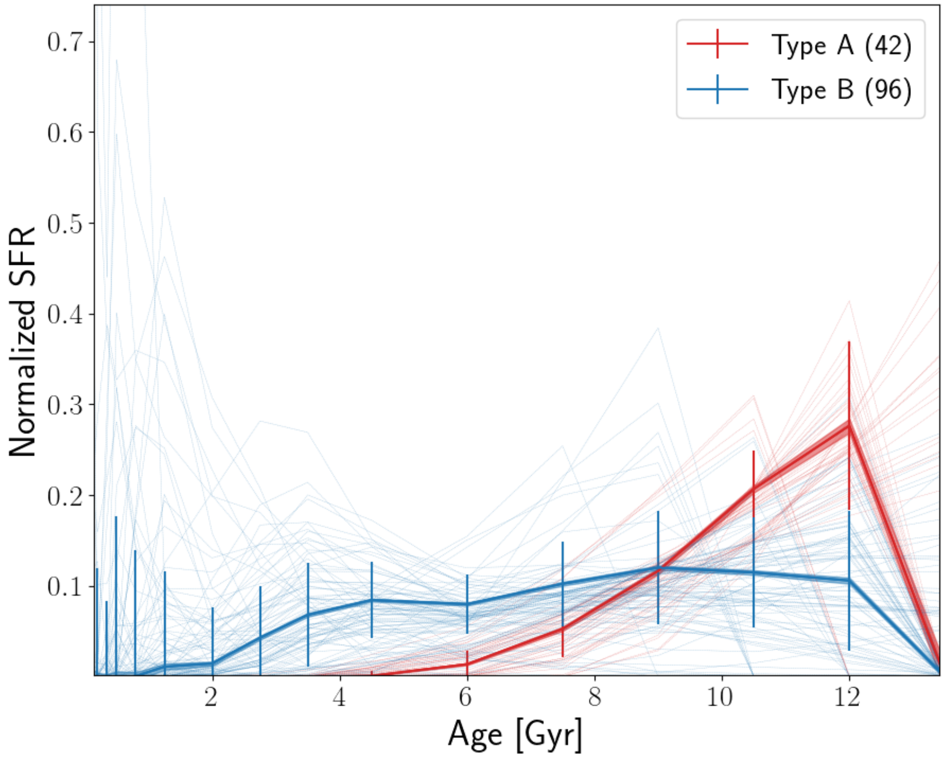

Figure 8: Normalized SFHs for empirical types A and B sources (red and blue lines, respectively). Individual sources are denoted by dashed lines, while population medians as solid lines. *Type A:* Sources with an exponentially, strictly decreasing SFR from an old single stellar population. *Type B:* Galaxies with extended, bimodal, or multi-peaked SFHs, typically in intermediate to young age epochs. Uncertainties are plotted as shaded areas and are obtained through a bootstrap method analogous to that defined in 3.3. Additionally, we plot the 1-σ dispersion of the SFR types along the y-axis as error bars. We highlight the number of sources in each category in the plot legend.

be contrasted with similar characterizations of the general galaxy population (which show a much starker bimodality between the blue cloud and red sequence).

To distinguish better the AGN hosts with flat or intermediate-age peaked SFHs, we separate the sample in two groups: Type A and Type B. For type A sources, their stellar population fits reveal a strictly exponentially decreasing SF from a dominant old (10–12 Gyr) population. In contrast, Type B sources show at least one additional SF episode at more recent epochs, that with peaks spanning a wide range of ages (e.g., $\sim$100 Myr, $\sim$ 1 Gyr or $\sim$ 4 Gyr). To further highlight the different SFH behaviors, we also show the median SFHs from the two types in Fig. 8. There is two main sources of uncertainty in this analysis: our limited aperture (we mainly trace bulges and central regions) and the age-dust-metallicity-AGN degeneracy problem which may be partly reflected in our observed deviations (see Fig. 8)

In 4.3, we correlate the presence of morphological signatures to the type of SFHs in our sample in order to establish any potential link between them.

3.6. *Emission-line fitting*

We subtract the best stellar continuum model from each galaxy to obtain the gas component's emission-line spectrum. We construct a `pyspeckit`-based code to perform a three-step fitting routine in the following manner: First, we fit the [OIII] lines, as these provide the highest S/N and are less contaminated due to them being isolated. We then use the [OIII] best-fit narrow widths to constrain the narrow components in the Hβ and Hα/NII complex, which are fit in a second step. Finally, based on a visual inspection and our χ^2 distribution, we add broad components (for Hα and [OIII]) in a few selected sources and re-fit based on the steps described above. We adopt theoretical line ratios throughout our routine to tie together the amplitudes of the [NII] and [OIII] doublet lines. We only use Gaussian models in our analysis, which appear to be sufficient for most sources. In our routine, we tie the widths of all the narrow lines and the widths of all the broad lines together. In practice, this method does not significantly increase fit residuals and allows to properly separate the narrow-line emission from the broad-line emission. The same is true for the broad components. The only parameter that links narrow and broad features together is the central rest wavelength, which we fix as being consistent for every line. We use rounded theoretical values for the relative widths and amplitudes of the lines using the [OIII] $\lambda\lambda$ 5007 line as a reference for the fit guesses. Except for two sources with no detectable Hα emission, we fit and compute $H\alpha$ for our whole sample.

We retrieve narrow line Hα fluxes to analyze further the star-formation properties derived from the optical emission and compare to that of the IR. To recover uncertainties on the fit parameters, we use a Monte-Carlo approach. We generate random Gaussian distributions with the same size as the number of pixels in our spectra, to be added as noise. To ensure this noise is comparable to the original spectral noise, we set their standard deviation and amplitude based on the continuum-subtracted spectra's global statistics: standard deviation and root mean squares. We ran a total of a 100 Monte-Carlo simulations for each galaxy's spectrum, and recovered their mean and standard deviation as confidence intervals.

3.7. *AGN classification and sources of ionization*

Emission lines are known for probing the warm ionized phase of the interstellar medium (ISM), and differences in line widths and ratios can be useful to determine the nature of the ionization mechanism, such as from AGN, post-AGB stars or shocks. One of the most widely used type-II AGN selection techniques is the so-called BPT diagram (Baldwin et al. 1981), which uses emission line-ratios to characterize the nature of the dominant photo-ionization mechanism present in the galaxy.

Such line diagnostics typically use comparisons between Balmer and forbidden lines, where the latter are sensitive to the strength and spectrum of the ionizing radiation. The most frequently used BPT ratios compare [OIII]/Hβ to [NII]/Hα and [SII]/Hα. Empirical (e.g. Kauffmann et al. 2003) and theoretical (e.g. Kewley et al. 2001) demarcation lines are used to separate AGN-based photo-ionization from ionization by young O and B-type stars.

Using our line measurements, we compute relevant line-ratios and plot our sample on the BPT diagram (Fig. 9). As expected, the BASS sources appear to be strong AGN, dominated by nuclear photo-ionization. Both demarcation lines

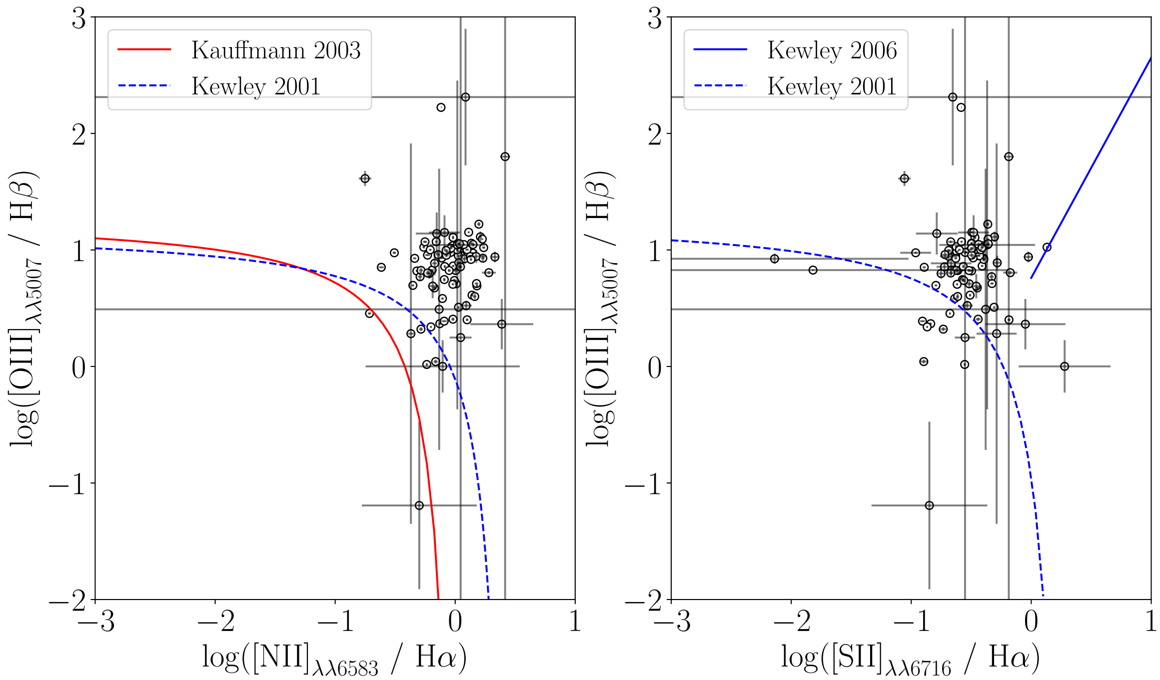

Figure 9: BPT diagrams showing [OIII] $\lambda\lambda$ 5007/Hβ versus [NII] $\lambda\lambda$ 6583/Hα ;((*left*) and [SII] $\lambda\lambda$ 6716/Hα (*right*) for our sample (black open circles with 1-σ error bars) . The curves correspond to the demarcation for HII and AGN photoionization given in Kauffmann et al. (2003, solid red) and Kewley et al. (2001, dashed blue). The solid blue demarcation line in the [SIIb]/Hα plot represents the separation between Seyfert galaxies and LINERs (Kewley et al. 2006). The vast majority of sources in the sample appear to have emission lines dominated by AGN photoionization.

show that our line ratios cannot be explained by the presence of young stars alone. According to the Seyfert/LINER/HII classification line presented in Kewley et al. (2006), and in contrast to normal optically selected galaxies HII class), the BASS AGN are dominated by Seyfert types. Because of the strong AGN ionization, Hα is very likely contaminated, if not dominated. For this reason, we consider the Hα measurements to be strong upper limits on the star formation and prefer whenever possible to use IR-derived star formation rates in our later analyses.

3.8. *Hα fluxes and FIR-derived star formation indicators*

Despite the AGN nature of our sample, we are keenly interested in the star-forming properties of the AGN hosts. However, due to strong nuclear photoionization, recovering star formation measurements from Hα-fluxes in AGN hosts may not be reliable. Fortunately, several alternatives exist (e.g, [OII] lines, SED fitting of infrared spectra). After properly accounting for AGN contributions, the use of far-IR (FIR) spectral measurements is perhaps the most robust method to measure the star-formation due to the low opacity at these wavelengths. We take IR-based SFR measurements from Ichikawa et al. 2019, who include deconvolved measurements of SF and AGN contributions to the total IR SED for a large subsample of BASS AGN, and use these throughout.

As mentioned in Sec. 2.3, the stellar mass measurements and the IR subsample (comprising data from WISE, AKARI, IRAS and Herschel, covering most of the infrared range up to 500 μm) are based on the older 70-month Swift-BAT

AGN catalog, and hence only partially overlap with our sample. As such, a crossmatch with our X-SHOOTER sample results in a significant down-selection to only 57 sources; this represents ≈32% of our original 180 source sample and $\lesssim$6% of the complete 105-month Swift–BAT AGN catalog. The IR subsample is largely unbiased for near and mid-IR based photometric measurements due to the high sensitivity of WISE. However, some of the IR SFR measurements can be highly uncertain due to more restricted, flux-limited FIR Herschel data. For consistency, and to avoid further biases, we assume all SFR measurements with no $> 25\mu m$ data are upper limits. As for stellar mass measurements, we do not expect them to introduce significant selection biases, since they are also dependent on the SED fitting of the mostly unbiased IR subsample. In addition to the above, we note that some unresolved interacting galaxy pairs have been removed from the IR sample due to confusion issues (see Ichikawa et al. 2019 for details).

Because not all AGN in our sample have FIR constraints, and a proper comparison to the optical measurements of SF might be important to determine the effect of dust in the optical regime, we also use a subset of Ichikawa et al. (2019) sources which have definitive *Herschel* flux measurements due to SF and have similar aperture (a PSF of 6″). This effectively corresponds to the more direct measurements and results presented in Shimizu et al. (2017). Thus, cross-matching our sample with Shimizu et al. (2017) allows us to establish optical versus IR measurements of SF, minimizing the need of strong multiwavelength calibrations.

We cross-match our sample to the *Herschel*-observed AGN sample of Shimizu et al. (2017) and compare the Hα-derived star-formation measurements against those from the infrared. As multi-instrument quantities, such a comparison might require an appropriate aperture calibration.

The maximum PSF of *Herschel*, from which Shimizu et al. (2017) derive measurements, is 6″. In contrast, the XSHOOTER spectra have an aperture of 1.6″ × 4″. To investigate possible differences due to aperture affects and assure we are tracing a similar region's star-formation, we statistically correct the XSHOOTER measurements based on the overlapping results of spatially resolved Hα emission in BASS AGN observed with MUSE (D. Kakkad, private communication) for two different orientations and three different aperture sizes. Based on three cross-matched sources from our sample plus 17 MUSE-only measurements of other BASS sources, orientation effects and overall differences are estimated and taken into account. In particular, due to aperture effects, XSHOOTER Hα fluxes must be corrected by a mean upward shift of ~ 0.3 dex to match the fluxes from MUSE for an aperture comparable to the PSF of *Herschel*.

We make a comparison of Hα-derived star formation rates ($\mathrm{SFR}_{H\alpha}$) and IR-derived star-formation rates (SFR_{IR}); here we again stress that the Hα-derived values are in effect strong upper limits, since the ionization of the sample appears to be almost universally AGN-dominated (see 3.7). We derive star-formation rates from both our Hα measurements and FIR-derived ones from Shimizu et al. (2017), following the standard Calzetti relations (Calzetti 2013, and assumptions therein):

$$\mathrm{SFR}_{IR} = 2.8 \cdot 10^{-44}\ \mathrm{L(IR)} \tag{1}$$

and

$$\mathrm{SFR}_{H\alpha} = 5.5 \cdot 10^{-42}\ \mathrm{L(H}\alpha) \tag{2}$$

Both star-formation rates are measured in $M_\odot$ yr^{-1} and the luminosities in erg s^{-1}.

To examine dust-extinction effects, we also compute Balmer decrements as Hα/Hβ ratios. Using the decrements and the theoretical value of this ratio ($R_{the} = 2.86$), we compute a color excess towards nebular regions as follows (Calzetti et al. 2000, Domínguez Sánchez et al. 2012):

$$\mathrm{E(B\text{-}V)} = \frac{2.5}{R_V(f(H\alpha) - f(H\beta))} \log \frac{R_{obs}}{R_{the}} \tag{3}$$

employing the extinction law of Calzetti et al. (2000) and their favored $R_V = 4.05$, and we correct our optical line fluxes and Hα-derived star-formation rate limits thereafter using the relation:

$$F_{corr} = F_{obs} 10^{0.4 R_V E(B-V)}. \tag{4}$$

3.9. *Hα measurements and comparison to the IR*

After computing SFR's and matching our data to Shimizu et al. (2017), we compare our derived quantities against those from the IR. As shown in Fig. 10 (*left*, there is a clear mismatch between the raw results by at least a factor of three, with some outliers reaching more than an order of magnitude discrepancy. We see a mild correlation between obscuration and optical versus IR SFR differences. We correct for dust extinction and aperture differences (described in Sec. 3.8) and plot our results in Figure 10 (*middle*). More sources move toward the 1:1 relation, but we still find that some of the SFR measurements are inconsistent within the estimated scatter for various outliers. A full compilation of the SFRs and extinction estimates are provided in Table 1.

3.10. *Lick Hδ_A, equivalent widths and D_n 4000*

To trace the light from intermediate age stars (A and F type), we compute Lick Hδ_A values using the `pyphot` (version 1.0) Python package. These are defined as the equivalent width of the absorption line at 4083.500–4122.250Å (Worthey 1994; Worthey & Ottaviani 1997). Strong Lick Hδ measurements indicate the end of hot O and B stars' evolution and can trace galaxies that had a burst of star formation $\sim$ 0.1-1 Gyr ago. Out of the 138 sources with good stellar population information as per section 3.2, we compute Lick $H\delta_A$ indices for only 130 of them because, in 8 cases, we solely had near-ultraviolet spectra instead of the whole wavelength band (see Sec. 2). We also use the `specutils` (version 1.1) package to retrieve Hα equivalent widths, useful to quantify star formation rates and potentially to characterize the ionization state (Cid Fernandes et al. 2011). Lick indices are computed on the spectra, whereas for the equivalent widths we define our best-fit continuum as a continuum estimate. In Fig. 11 we see that most of our sources lie in the EW($H\alpha$) > 10 Å region, consistent with most optically-selected studies. However, to

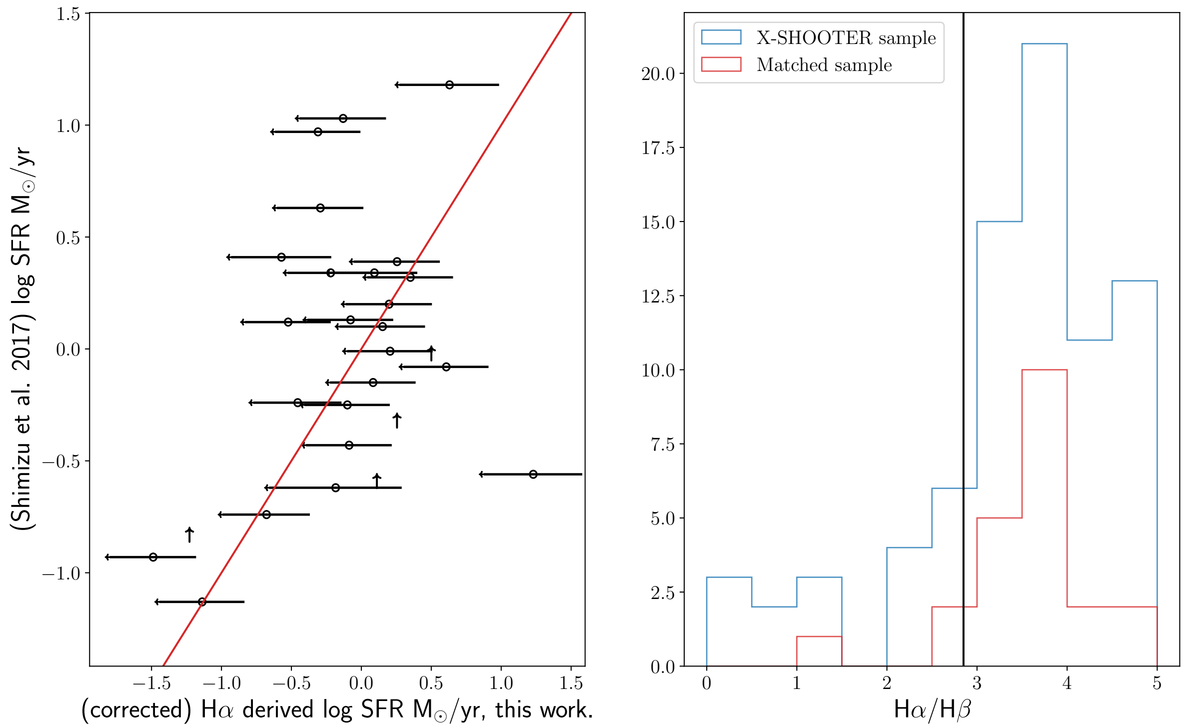

Figure 10: (*left*) Comparison of SFR measurements (detections and upper limits) derived from optical spectra (this work; aperture and extinction-corrected) and IR methods from Shimizu et al. (2017). The red lines denote the 1:1 relation. (*right*) The Balmer extinction measurement distribution.

keep sources with low ionization signatures, and in contrast to most optical studies, we still keep some sources (5) with weak Hα signatures.

The Balmer break strength at 4000Å is consistently used as a proxy for the mean stellar population age, as it directly probes the temperature of the stars forming the continuum. The D_n4000 index is one of the two most utilised indicators to measure the Balmer break strength. It is found computing the ratio of the flux in two spectral windows near the break: 3850–3950Å and 4000–4100Å (Balogh et al. 1999). We compute D_n4000 measurements for our sample using regular integration of the original spectra over the spectral regions defined above.

3.11. *Morphology analysis and classification*

We briefly outlined the importance of mergers in the introductory paragraphs. To better quantify the state and amount of gas in galaxies, which is a deciding factor in galaxy evolution, we classify our sample morphologically. This should give us additional insight into the nature of AGN hosts, their past, and potentially any link to their present star formation properties. When spatial resolution allows, we want to not only distinguish between elliptical and spiral hosts, but also look for any morphological signature that resembles signs of past interactions, as this may be an equally important feature when compared to primary morphology.

Using available archival imaging data, we perform a morphological classification based on the following two-tier scheme. For all sources, we assign a Primary class that defines the basic visual morphology of the object (i.e.,

(1) BAT index	(2) Name	(3) Swift counterpart name	(4) $log(\mathrm{SFR_{IR}})$	(5) $log(\mathrm{SFR_{opt,corrected}})$	(6) $log(\mathrm{SFR_{opt}})$	(7) Av (optical)
72	NGC526A	SWIFT J0123.8-3504	-0.62	-0.19	-0.89	1.02
114	ESO197-G027	SWIFT J0211.1-4944	0.97	-0.31	-0.74	0.31
153	NGC1125	SWIFT J0251.6-1639	0.10	0.15	-0.94	1.97
159	ESO417-G006	SWIFT J0256.4-3212	-0.74	-0.68	-0.97	-0.03
182	MCG-01-09-045	SWIFT J0331.4-0510	-0.93	-1.49	-2.04	0.64
193	ESO201-4	SWIFT J0350.1-5019	0.34	-0.12	-0.91	0.98
217	ESO157-G023	SWIFT J0422.7-5611	0.34	0.07	-0.35	0.36
247	ESO033-G002	SWIFT J0456.3-7532	-0.25	-0.10	-1.01	1.52
258	2MASXJ05054575-2351	SWIFT J0505.8-2351	-0.43	-0.09	-0.49	0.26
509	2MASXJ10402231-4625	SWIFT J1040.7-4619	0.45	-2.53	-1.57	-3.17
630	LEDA170194	SWIFT J1239.3-1611	0.32	0.35	-0.31	0.89
653	NGC4941	SWIFT J1304.3-0532	-1.13	-1.14	-1.89	1.13
654	NGC4939	SWIFT J1304.3-1022	0.12	-0.52	-1.13	0.77
669	NGC5100NED02	SWIFT J1321.2+0859	1.18	0.63	-1.00	3.33
677	ESO383-18	SWIFT J1333.5-3401	-0.56	1.23	-1.36	5.71
751	IC4518A	SWIFT J1457.8-4308	0.63	-0.29	-0.91	0.80
772	MCG-01-40-001	SWIFT J1533.2-0836	0.41	-0.57	-0.71	-0.41
823	ESO137-G034	SWIFT J1635.0-5804	0.13	-0.08	-1.23	2.12
836	LEDA214543	SWIFT J1650.5+0434	-0.15	0.08	-0.99	1.94
970	IC4709	SWIFT J1824.3-5624	-0.24	-0.46	-1.22	1.15
988	ESO103-035	SWIFT J1838.4-6524	-0.08	0.61	-0.73	2.60
1092	IC5063	SWIFT J2052.0-5704	-0.01	0.20	-0.79	1.73
1097	ESO464-G016	SWIFT J2102.6-2810	0.39	0.25	-0.46	1.04
1174	UGC12237	SWIFT J2254.2+1147B	0.20	0.20	-1.24	2.83
1198	NGC7682	SWIFT J2328.9+0328	1.03	-0.13	-0.73	0.73

Table 1: IR-derived SFR measurements from Herschel (Shimizu et al., 2017) versus optically derived SFR for all our cross-matched sources. We provide extinction measurements and corrections based on Balmer ratios (see subsection). Note that both dust-corrections and aperture-corrections are made (they amount to $\sim +0.3$ dex on average). See Sec. 3.8 for details.

elliptical, spiral, indeterminate, or point-like). This can be achieved reliably even with relatively poor image quality (e.g., even with DSS or unWISE). Additionally, for a subset of sources, we assign a Secondary class that relates either to the dynamical state of the source (current merger, merger remnant, tidal tails, presence of either interacting or not-interacting companion) or an apparent visual feature of the same object (edge-on galaxy). Naturally, secondary classifications are largely possible only in the higher resolution and/or more sensitive SDSS, PanSTARRS and DESI Legacy cutouts. Thus, a correction should be made when discussing the overall number of sources with morphological features within our sample; comparing classifications with different resolutions and sensitivities allows us to assess what types of the morphological details (and fractions thereof) are either lost or accounted for when performing a visual classification.

Examples of our morphological classification can be found in Figs. 1 (spiral plus companion) and 2 (elliptical, merger remnant). Additionally, to have an idea of our bias against morphological features in low resolution data, we include a pie-chart of some of our results in Fig. 3. The latter plot shows both the relative percentages of high and low resolution data present in our sample, and a rough measure of the bias regarding having some sources with no available deeper resolution images: in our subsample that only has low resolution cutouts, we only detect morphological features (a secondary classification within our scheme) in $\sim 17\%$ of the total subsample. For the high resolution one, this value ascends to $\sim 45\%$. This implies that some fraction of our sources likely have trace features of past interactions, yet lack

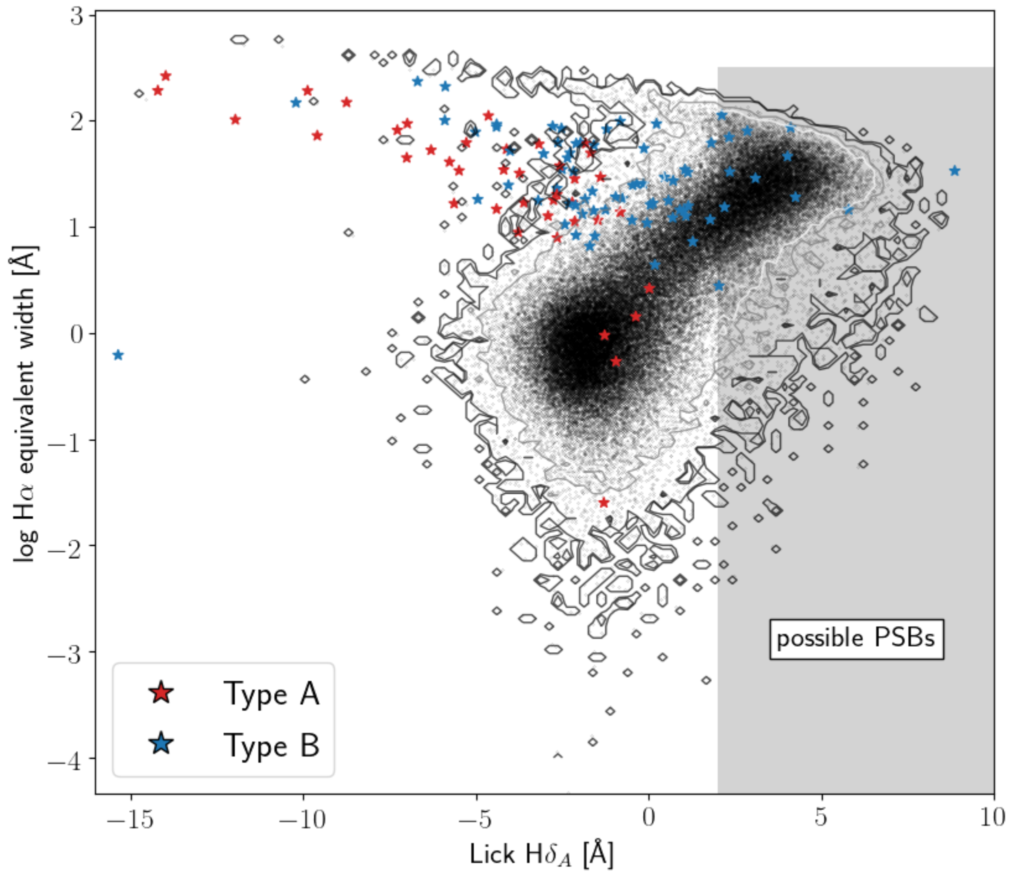

Figure 11: Lick Hδ_A measurements versus log EW(Hα) for 112 AGN from the X-SHOOTER sample. We plot the SDSS comparison sample (see 3.12) as black dots and our sample as blue and red stars. Red stars ('Type A') correspond to sources with a single decaying star formation peak at old ages (> 10 Gyr), whereas blue stars ('Type B') correspond to every other type of SFH. Section 3.5 provides more details regarding our SFH classification. In gray, we highlight the nominal region adopted to select PSB candidates for our study. As revealed by our diagnostic diagrams, our sample contains high levels of AGN ionization and thus all of the $H\alpha$ measurements should be considered strong upper limits.

a secondary classification due to the current best image depth. Based on the fraction of low-resolution, shallow-depth imaging, we estimate at least an additional 7% of the total sample likely have dynamical features.

3.12. *Comparison sample*

To interpret and place our results in context, we construct a comparison sample from the SDSS DR7 data and the MPA-JHU catalog. From the MPA-JHU catalog, we extract Lick Hδ_A, Hα and Hβ line fluxes, stellar masses, redshifts and D$_n$4000 values. We make cuts to match our sample in redshift ($0.01 < z < 0.3$) and stellar masses ($9 < M_* < 12.5$). We also perform quality control cuts in signal-to-noise (S/N) ratios per pixel of the integrated spectrum (S/N > 10) and Hα equivalent width (EW) errors (err Hα EW > -1) measurements.

To address possible cross-calibration issues related to mixing XSHOOTER and SDSS measurements, we construct an SDSS calibration sample. We match 15 BASS SDSS galaxies with reliable spectra to the MPA-JHU catalog, and apply our pipeline to it. We find overall consistent values for our measured parameters. In particular, after a systematic +0.1 calibration in the measurement for our D_n4000 index, we find mean variations of ≈ 0.05 dex for our D_n4000 measurements for our matched SDSS sample when comparing to the MPA-JHU catalog. We do not calibrate our EW(Hα) measurements, nor our line fluxes or Lick Hδ_A values. For EW(Hα) we only find small variations at low equivalent widths with a mean ≈ 0.08 dex, whilst Lick Hδ_A and Hα fluxes are very consistent with differences of ≈ 0.013 dex and ≈ 0.08 dex respectively. Overall, most differences in all measurements fall within ≈ 0.1 dex with some variance at high Hα fluxes or low equivalent widths.

4. RESULTS

4.1. *Basic host properties*

After applying the techniques and procedures described in Sec. 2 to all of the available host galaxies in our sample, we retrieve useful quantities such as mass-weighted mean ages and metallicities (see Fig. 23). Our results show that the stellar populations in the central portions of the galaxies probed by the XSHOOTER spectra are predominantly old and metal-rich and have relatively low (luminosity) contributions from O and B-type stars, as demonstrated by low Lick $H\delta$ measurements in Figs. 11 and 20. This is what one might expect from relatively massive ellipticals or spirals with substantial bulges, which have been previously demonstrated to preferentially host bright AGN (e.g. Kauffmann et al. 2003).

We note that a large fraction of our sample present a broad distribution of stellar ages. Any instances of relatively recent star formation are critical to investigate possible quenching effects. To quantify this, we characterize the SFHs using 20th percentile and Hδ measurements, as shown in Figs. 14 and 20, and conclude that both tracers are, aside from a few outliers, consistent. Fig. 11 shows that the bulk of the AGN sample have rather low Lick Hδ_A values, with 8 outliers being within our cut of Lick H$\delta_A > 2$. We consider galaxies which have substantial $\lesssim 1$ Gyr old stellar populations as the primary candidates for our PSB selection.

4.2. *Comparison to AGN properties*

We compare our derived results to Koss et al. (2017) to look for potential correlations between SFH tracers and AGN Eddington ratios and BH masses. Figures 12–14 show the results of this comparison: no significant trends are found for various SFH percentiles or Lick Hδ indices. As our sample selection does not cover all Eddington ratios and BH masses parameter space, we also plot the whole BASS sample as black dots.

4.3. *Host Morphologies and Evolutionary States*

We use the methods described in Section 2.2 to classify galaxies in our sample into one of the three main primary classes: ellipticals, spirals and indeterminates. Our results indicate that $\approx 58\%$ (75) of our sources are spirals, $\approx 30\%$ (39) are ellipticals and the remainder $\approx 12\%$ (15) is comprised of indeterminate galaxies. After our primary morphological classification, and as previously described, we decide to split our sample in a secondary classification. This separates sources that have dynamical morphological features (mergers, merger remnants, tidal features and close

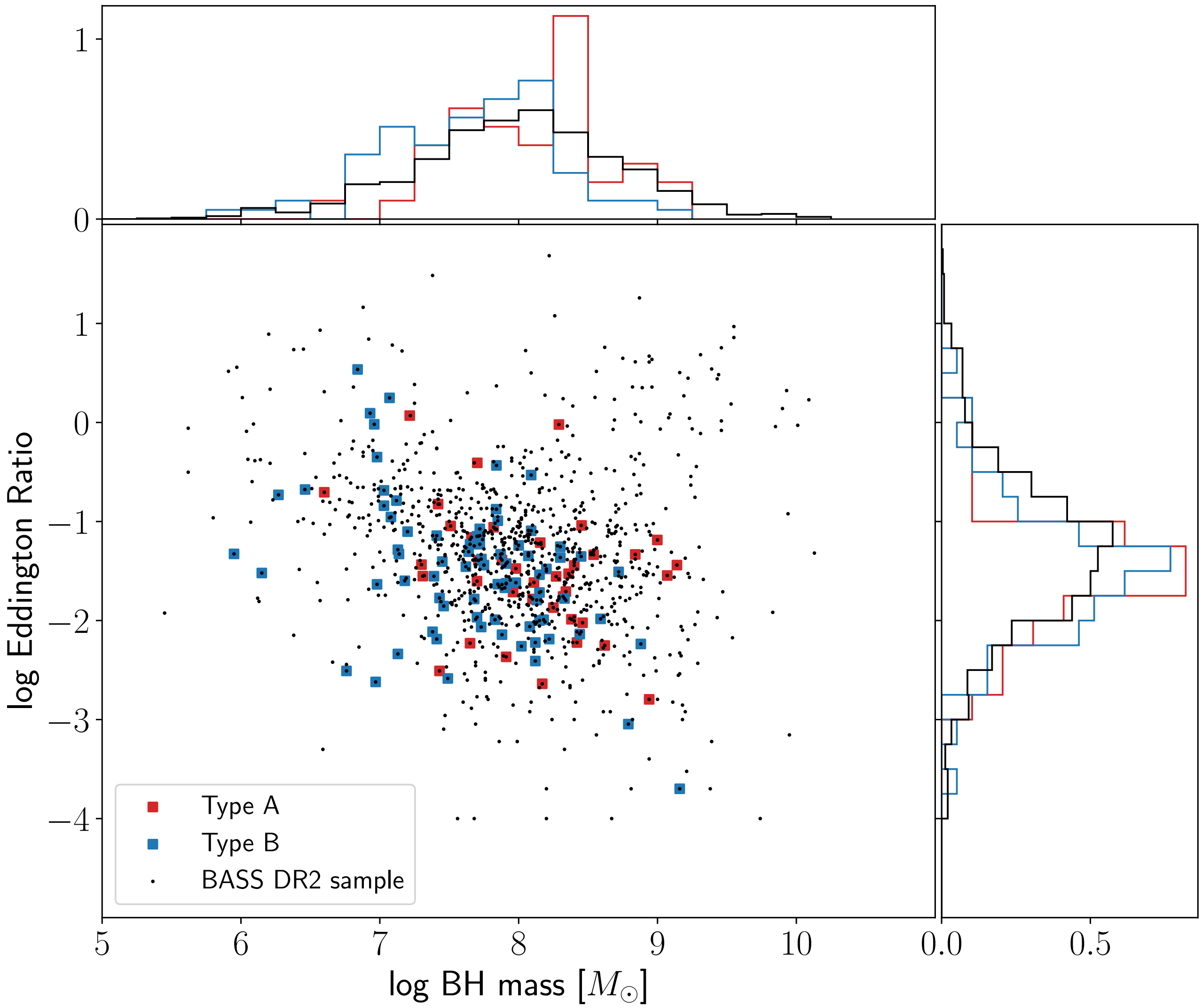

Figure 12: Comparison of BH mass versus Eddington Ratio, as a function of SFH type. Type A sources with an old (> 6 Gyr) single-peaked stellar population component are shown in *red*, while type B sources with flat or doubly-peaked (one peak < 6 Gyr) stellar population components are shown in *blue*. The entire BASS DR2 sample are shown as black dots for comparison.

companions), and those that do not present them, given the spatial resolution in the image cutouts. To study the past of each class, we decide to use our stellar population synthesis results to track the shape of median SFHs and their possible starburst episodes.

Figure 15 shows the results of our classification when visualizing the global SFH of each subset. Interestingly, we only see mild differences in the median SFH of elliptical/S0 compared to spirals, and we even see slightly higher SF at intermediate ages in the elliptical/S0 sample. This may be related to the fact that our spectra are mostly tracing the spheroidal component of both types, In contrast, when we separate sources according to the secondary morphological classification, we see much clearer differences in the median SFH between both groups, whereby the sources having no dynamical features almost completely resemble the expected SFH of typical red-sequence ellipticals, even though

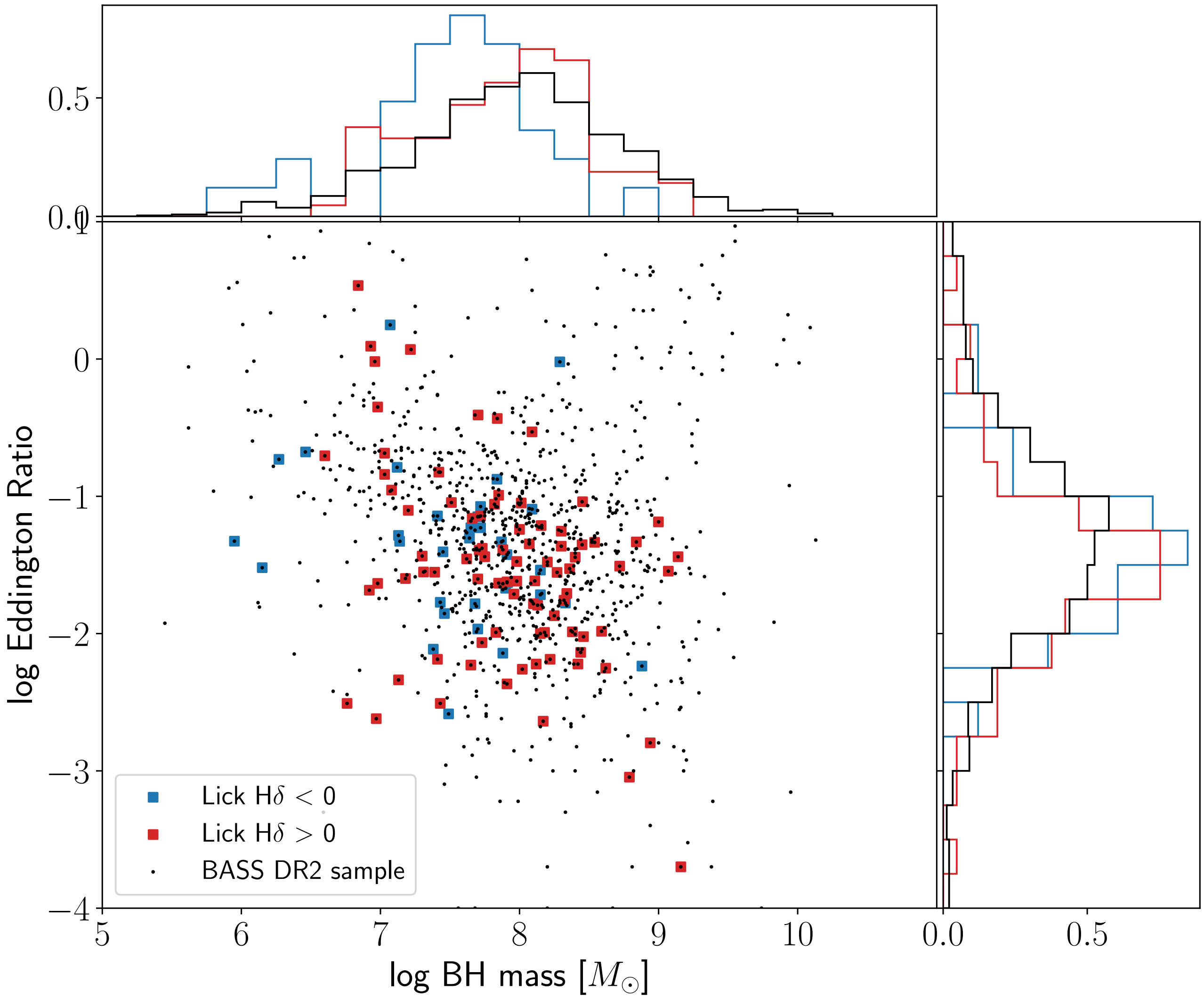

Figure 13: Same as Fig. 12, but *red* sources denote Lick indices $H_\delta < 0$, while *blue* sources denote Lick indices $H_\delta < 0$

.

there is a significant fraction of spiral galaxies in this group (see Fig. 16). In addition to this, we note the similarity between the average SFH of the dynamical feature and Type B samples, and the non-interacting and Type A samples. Therefore, we look for a correlation and links between these in the simple evolutionary scheme we present here.

When using the mean instead of the median, we notice the effect of outliers in the overall shape of the SFHs. The presence of sources with intermediate-age starbursts tends to drive similar mean SFHs when sorting galaxies by their secondary classification. This could partly be due to some false-positive sources with dynamical features that are not well resolved at their image depth. Some of these outliers can also correspond to PSBs.

A complete picture for galaxy evolution should include evolutionary tracks for sources with different redshifts, stellar masses and morphologies through the colour-colour diagram or analogous schemes. In particular, the stellar mass versus SFR diagram provides a physically-oriented medium to characterize the evolution of galaxies through some

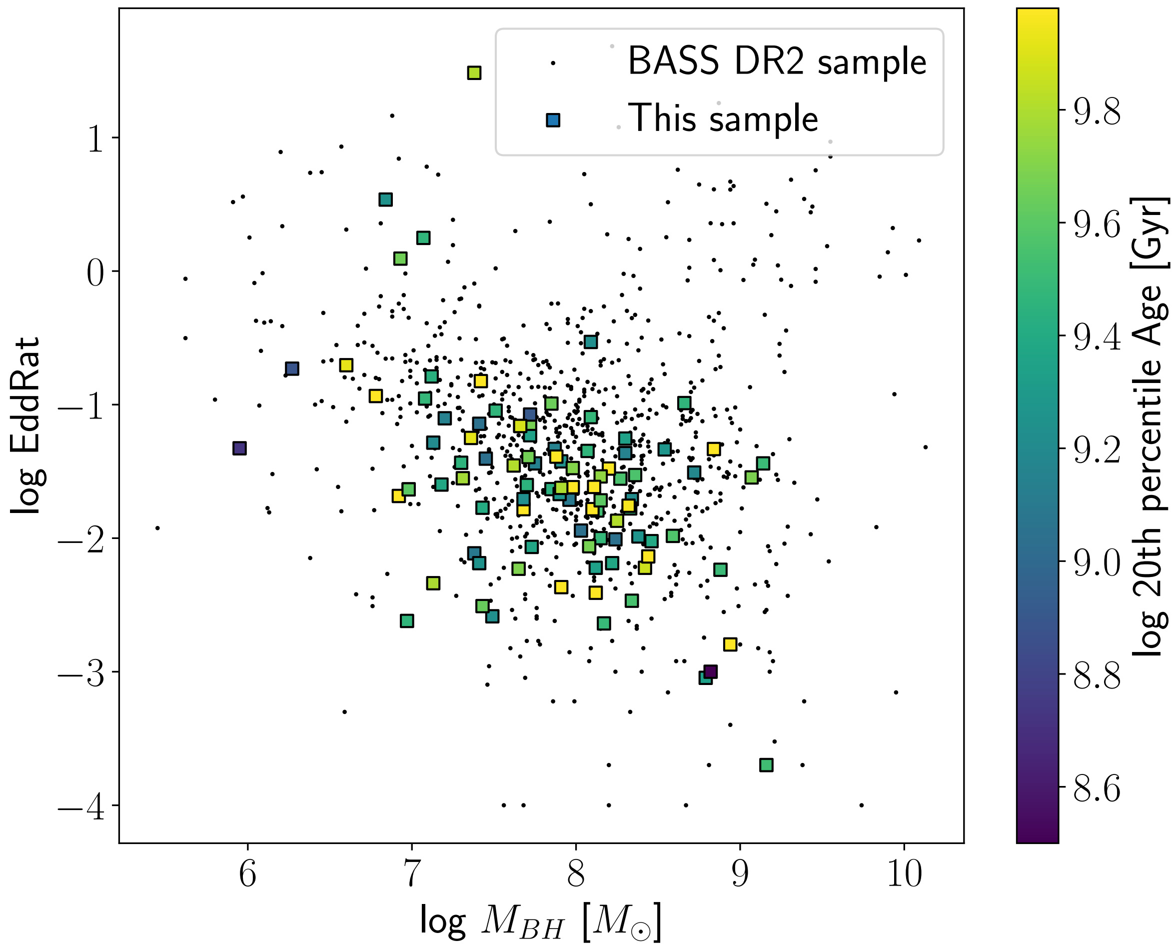

Figure 14: Same as Fig. 12, but sample sources are now color-coded by their 20th percentile SFH ages.

of the most relevant regions in the colour-colour diagram. These bands naturally correspond to the main sequence (MS), the red sequence (RS) and the green valley (GV), which have analogous regions when using the stellar mass versus SFR picture.

Nevertheless, the use of tracks is limited to sources with reliable SF through all their past including their current SF. Because our low number of sources with reliable current SF tracers (our IR-subsample), we decide to use a different approach to broadly characterize evolution. Using a similar method to (Schawinski et al. 2014) we construct and split a diagram (in our case, the stellar mass versus SFR diagram) into morphologies (spiral, elliptical/S0 and indeterminate) and also into three main bands (MS, RS and GV), and use number counts in each band to provide a basic scenario that aims to explain the current distribution of sources in the diagram. We note, however, that due our currently low-number statistics, some of the results in the following section will have significant uncertainties, and should be made more robust in a near future work. Despite the above, we decide to undergo this analysis as a first step for a reliable and relatively unbiased picture for the evolution of AGN hosts through the BASS sample.

(1) Category	(2) Total Fraction	(3) Type A	(4) Type B	(5) Dynamical	(6) Non Dynamical
SB Spirals	13.6 % (6)	33,3 % (2)	66,7 % (4)	83,3 % (5)	16,7 % (1)
MS Spirals	45.5 % (20)	25 % (5)	75 % (15)	30 % (6)	70 % (14)
GV Spirals	13.6 % (6)	83,3 % (5)	16,7 % (1)	16,7 % (1)	83,3 % (5)
Total (Spirals)	72.7 % (32)	37,5 % (12)	62,5 % (20)	37,5 % (12)	62,5 % (20)
MS Ellipticals	6.8 % (3)	0 % (0)	100 % (3)	66,7 % (2)	33,3 % (1)
GV Ellipticals	13.6 % (6)	16,7 % (1)	83.3 % (5)	66,7 % (4)	33,3 % (2)
RS Ellipticals	6.8 % (3)	100 % (3)	0 % (0)	66,7 % (2)	33,3 % (1)
Total (Ellipticals)	27.2 % (12)	33,3 % (4)	66,7 % (8)	66,7 % (8)	33,3 % (4)

Table 2: Breakdown of source morphologies and evolutionary states for the 44 sample galaxies with reliable stellar mass and IR-SFR measurements shown in Fig. 16. Total fractions (%) and numbers (in parentheses) of galaxies listed according to our SF band and morphological classification categories. For red sequence galaxies, we incorporate usable optical SFR upper bounds (see subsection) *Column 1*: Rows represent each of the six main categories we use throughout the analysis. *Column 2*: total fractions (and numbers) of galaxies for each category. *Columns 3-6*: specific fractions and numbers of galaxies present in each SF band and morphological category.

As a comparison, and to populate our stellar mass versus SFR diagram, we use our comparison sample from the MPA-JHU catalog. Additionally, we define delimiters for each of the three main bands (see Appendix 6.2 for the specific definition). These limits are made in a way that improves the overall number statistics along three bands, while also being similar (albeit not equal) that most modern studies. Based on these bounds, we define six main regions in the stellar versus SFR diagram (*1* in Tab. 2): starburst (SB) spirals, MS spirals and GV spirals for spiral galaxies and MS ellipticals, GV ellipticals and RS ellipticals for elliptical galaxies.

In Fig. 16 we investigate the stellar mass and IR-SFR properties of our sample subset, at least for the subset with such measurements, as a function of their specific morphologies and secondary classifications. Broadly speaking, we find our results in stellar masses and SFR consistent with Kauffmann et al. 2003; Koss et al. 2011, e.g., and Koutoulidis et al. 2021 respectively. Overall, we find a very high number of high SF ellipticals compared to our control sample, with almost all being in the green valley and some of them even in the main sequence band. Their SFH, having quenched their intermediate populations at earlier epochs, support the idea of them being transitional sources between spirals and regular green valley ellipticals. Spirals, overall, have a more predictable placement in the stellar mass-SFR diagram. However, we see a mixed behaviour in the sense that some of them have very high SFR and signs of past merger events, but most of the lower SFR spirals do not present these features despite their SFH type classification, particularly those in the green valley. Our small sample of indeterminates does not seem significantly different from either the elliptical/S0 distribution or the spiral one. In the figure, we highlight the high correlation between Type A galaxies to the subset with no dynamical signatures and viceversa. In Fig. 18, we also note the overall increase in mean SFR for the later samples along all the three SF bands. Table 2 shows the relative fractions of each sub-class of galaxies present in each of the main bands in the SFR versus stellar mass diagram. Despite our low-number statistics, we can see the following picture:

- Spirals ($\sim 70\%$ of M_*-SFR sub-sample) show a variety of different behaviors. Firstly, we note a predominance of Type B and dynamical-feature galaxies for spirals just above the main sequence (starbursts; SB). SB-spirals tend to be among the galaxies with the strongest tidal features and dynamical structures such as tails. The above evidences, coupled with their SFH types, their positioning in the diagram and their clear differences to their neighbours in other SF bands (see below) suggest recent mergers as the primary reason behind their enhanced SFRs. In contrast, main-sequence (MS) spirals and green valley (GV) spirals show significantly different behaviors. MS spirals show a predominance of sources without dynamical features, especially on the bottom part of the band. Despite mergers and close companions not being the majority here (Dynamical featured sources comprise $\sim 30\%$), 75% of these galaxies present complex, Type B SFHs. i.e., their younger population components are outshone by the oldest stellar population, but we still do see them in their histories. This suggests a scenario in which at least 70% of the spirals in this SF band are evolving via either environmental processes or secular evolution with minor (unresolved) interactions, but which nevertheless involve the generation of at least one minor starburst at intermediate epochs (1–4 Gyr). For GV spirals, we see a clear predominance of Type A SFHs with no signs of dynamical interactions, implying a completely secular evolution for about $\sim 80\%$ of the sources in this category. Overall, according to Table 3, $\sim 40\%$ of spirals show signs of mergers or other strong dynamical effects, while $\sim 60\%$ appear to be passively evolving through the main sequence and green valley and/or had only minor starbursts episodes in their past.
- For ellipticals ($\sim$30% of the M_*-SFR sub-sample), we see strong dynamical features and a high fraction of Type B SFHs in both the MS and GV, suggesting that $\sim$2/3 of ellipticals are either rejuvenated or in the final stages of star formation associated with a recent merger event. In contrast, a third of the ellipticals are completely devoid of significant SF (i.e., red-and-dead), and solely characterized by a strong SF peak at early epochs and no dynamical features in their images.

4.4. *The inclusion of optical SFR limits*

As previously shown in Sec. 3.7, our whole science sample is almost totally comprised of strong AGN with clear signs of AGN photoionization. However, our optical-SFR versus IR-SFR comparison suggest only minor differences (~ 0.3 dex, consistent with aperture uncertainties) between both measurements at low-to-mid SFR levels (log SFR < 0.5). Motivated by this empirical evidence, we decide to use our optical measurements of SF as upper limits to construct a second version of Fig. 16, which includes optical bounds for every source in our science sample which do not present IR measurements (either well-constrained or upper-limits only) and have log $\mathrm{SFR}_{\mathrm{opt,\,corrected}} < 0.5$. Naturally, this new analysis improves on our low number statistics, with the partial disadvantage of having increased uncertainties for our SFR limits. We plot this result in Fig. 17 for spirals and ellipticals, and in Fig. 21 for indeterminates (in Appendix).

4.5. *Are PSB special?*

To complement the above analysis, we focus briefly on the PSBs as selected and classified by our previous Lick $\mathrm{H}\delta_A$ selection criteria or by SFHs showing a second peak at ~ 1 Gyr. We find that both measures (Lick indices and SFH

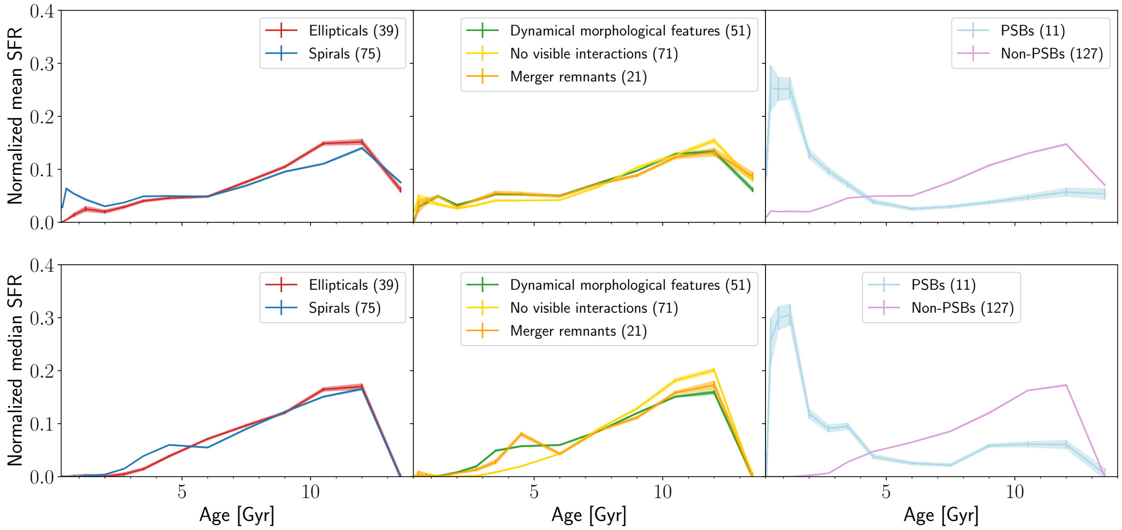

Figure 15: Normalized mean and median SFHs for several subsets in our sample. In all subplots, we plot uncertainties as error bars and shaded areas which are obtained through a bootstrap method analogous to that defined in 3.3. In the legend, we also include the number of hosts in each subset. As stated in the main text, Ellipticals and Spirals correspond to a primary classification (left), whereas 'Dynamical morphological features' and 'No interactions' correspond to a secondary classification (middle). In orange, we plot a subset of the 'Dynamical morphological features' set as an example ('Merger remnants'). We also include SFHs for PSBs and non-PSBs (right).

at sub-1 Gyz epochs) are very consistent, and almost all sources with high Lick Hδ_A also present intermediate age populations. Finally, we plot the median SFH of our selection in 15, along with the SFHs of galaxies with different classifications. Overall, we find that most of our PSB sample falls in the subset sample with morphological features resembling interactions of past merger events (8/12). We note that we do not have high-resolution cutouts for the 4 outlier sources that do not present these features. Despite our small sample and thus somewhat inconclusive results, this suggests a scenario in which most or all PSBs are a result of past merger episodes. We note that their Primary morphological classifications cover all types (S0, I, E, S), supporting the idea that they are in a broad range of transitional state.

It is also interesting to study the possibility of the AGN contributing to the quenching of these PSBs. However, in Fig. 15 we note that like most other galaxies, we are unable to reconcile AGN feedback directly to the quenching of their intermediate-age population due to the quenching timescale (~ 0.5 Gyr), although it is closer to typical AGN duty cycles compared to the rest of our sample. Interestingly, in Fig. 13 we note that there is a mild bimodality between low and high Lick$H\delta_A$ in the BH mass distribution. This might hint at feedback at more recent timescales (< 300 Myr), currently not accounted for.

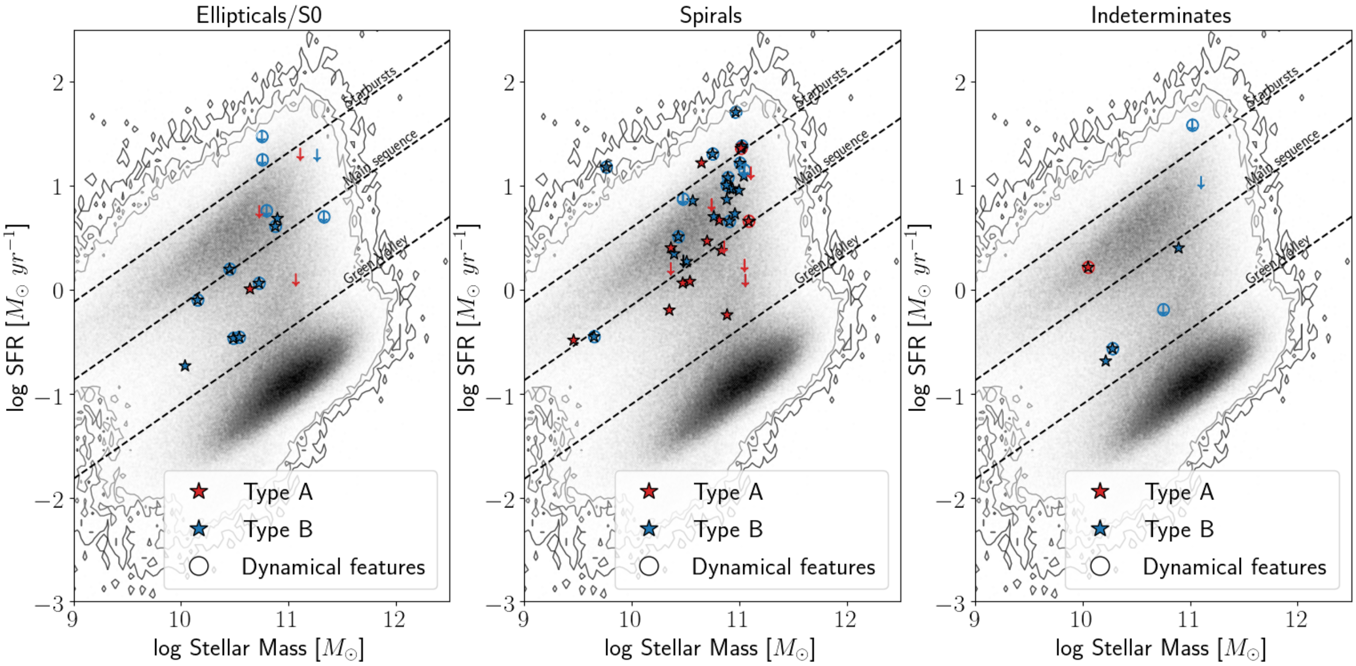

Figure 16: Comparison of IR-based SFR vs. stellar mass for the subset of sources with such measurements, split into panels by Primary morphological classification. *Red:* Sources with a single stellar population peak at old ages (> 6 Gyr, Type A sources) *Blue*: Every source that does not enter into the former classification (Type B sources). Primarily comprised of sources which show evidence of intermediate or young stellar populations, in addition to an older one. *Dashed lines* denote, from top to bottom, boundaries for the starburst, main sequence, green valley and red sequence SF bands, respectively. *Encircled markers* denote sources that present dynamical interaction features (signs of merger remnant, merger, tails or close companions).

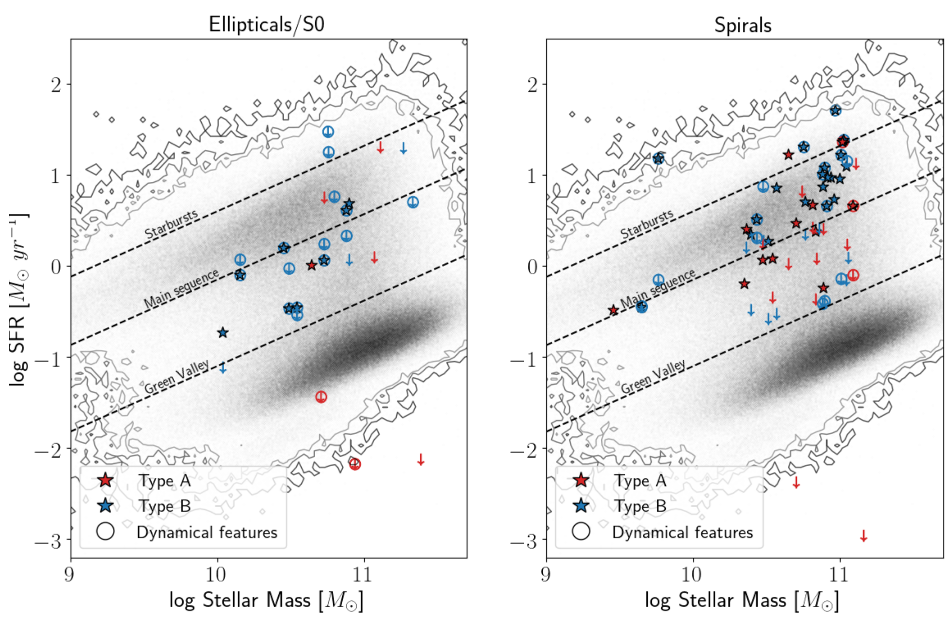

Figure 17: Same as Fig. 16, but with the inclusion of (dust and aperure-corrected) optical limits as per Sec. 4.4. These additional sources tend to populate the GV and, in a few instances, the RS.

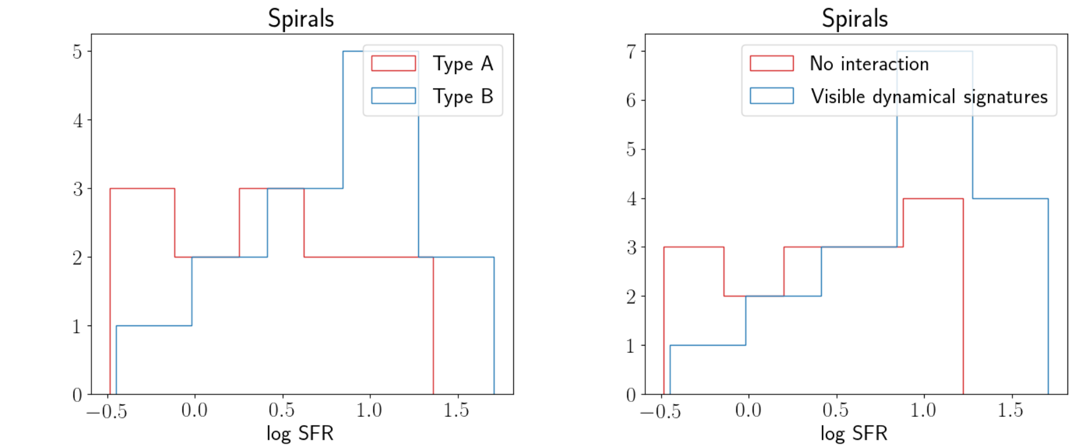

(a) (b)

Figure 18: Total number of sources within various SFR bins. *Left:* SFRs for Type A (red) and Type B (blue) sources over all the three Late-type bands.*Right:* SFRs for sources with no visible dynamical interaction signatures throughout our image cutouts (red) versus those that do have them (blue). Despite the small sample, we note a significant difference in the mean SFR for each case, with the blue sub-samples having an overall higher SFR.

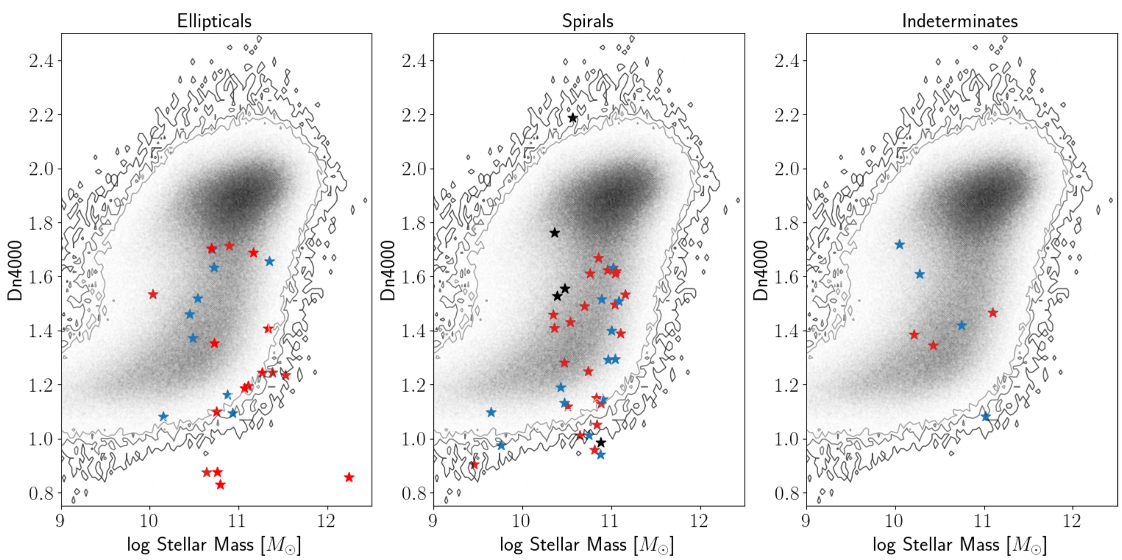

Figure 19: Comparison of Dn4000 vs stellar mass for the subset of sources with such measurements, split by morphology. *Blue* indicates sources with dynamical interaction features (signs of merger remnant, merger, tails or close companions). *Red* sources appear mostly isolated, with no visible morphological features that resembles any of the above examples. *Black:* Edge-on spirals.

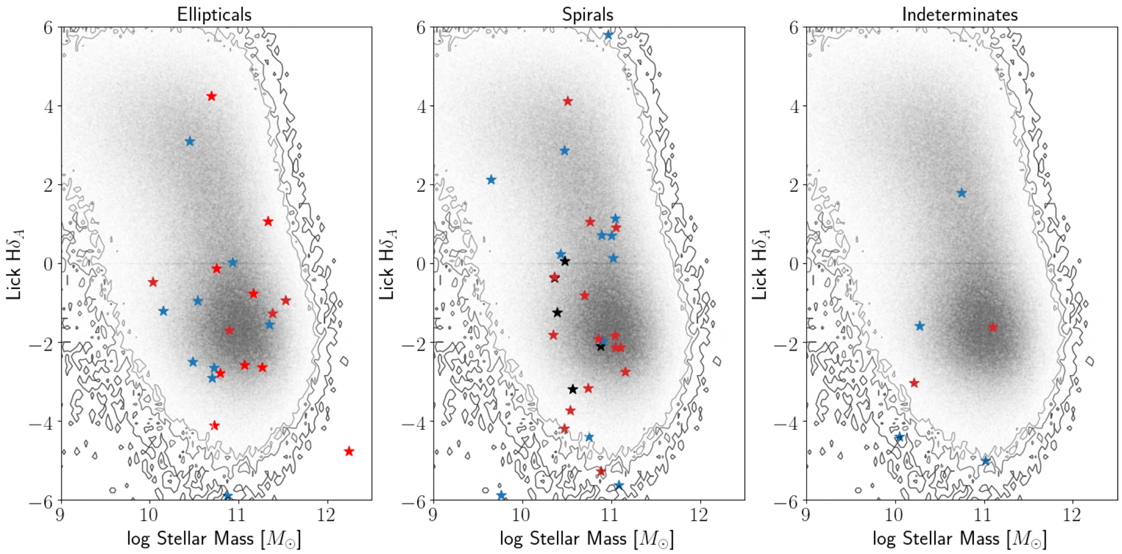

Figure 20: Comparison of Lick Hδ_A vs stellar mass for the subset of sources with such measurements, split by morphology. *Blue* indicates dynamical features (signs of merger remnant, merger, tails or close companions). *Red* sources that appear mostly isolated, with no visible morphological features that resembles any of the above examples. *Black:* Edge-on spirals.

5. DISCUSSION AND CONCLUSIONS

We conclude that our AGN sample (and by extension most local Type-II AGN in general) tend to be predominantly hosted by massive, star-forming galaxies. Despite their central regions being old and having formed most of their stellar mass at the cosmic noon, many present intermediate-age populations, often correlated to past merger episodes based on faint morphological features. Even though our Hα measurements are unable to properly measure the sample's current star formation, we see an overall agreement of our measurements compared to the IR. This is supported by both our SFR$_{IR}$ versus SFR$_{H\alpha}$ measurements and our SFH analyses and other indicators. Despite of the above, we do find some outliers at high optical SFR. This may point to the presence of SF hidden by dust, but we cannot completely ignore the possibility of systematic errors when we only have 15 sources for calibration purposes.

In practice, when compared to previous studies based on optical photometry (see e.g, Schawinski et al. 2009), the increased SFRs based on IR data drives most ellipticals AGN hosts up to the GV, and most of the AGN spirals to the MS. In comparison, our analysis is more consistent with the SFR distribution present in Koutoulidis et al. 2021 based on SED fitting methods. The slow decays in most SF episodes do not require major AGN feedback to the explained, and regular galaxy processes are likely sufficient (stellar feedback, secular evolution, exhaustion of gas reservoir after a dynamical interaction). However, we cannot rule out the possibility of AGN having a major role in the quenching of SF in the past, or recent ($<$ 300 Myr) times. The lack of a clear correlation between AGN properties and stellar populations/Lick indices suggest that there is no easy, direct causal link between AGN high-energy emission and star formation. We are inclined to support the hypothesis that there are other properties (e.g, gas content) that ultimately drive both the SMBH growth and star formation.

Figures 15 and 16 highlight that a significant fraction of sources in our sample have had visible dynamical interactions in the not so distant past (nearly 40%), and also complex SFHs defined by more than peak of past star formation (more than 50%). Outside the main sequence, most Type A sources have no visible interactions while most Type B sources show signs of dynamical interactions. Early-type AGN hosts appear to have enhanced SFR compared to the control sample, and we see few ellipticals in the red sequence. Given the high fraction of elliptical mergers and remnants within the green valley, it may be the case that while the galaxy reassembled into an elliptical on ∼1 Gyr timescales, larger scale gas (perhaps associated with tidal tails) may take longer to accrete back onto the galaxy, potentially powering the past/current SFR to some extent, by the enhancement of gas supply or red sequence ellitpicals. A closer look at correlating SFH properties to the specific morphology and related timescales, as well as observations aimed at quantifying the amount of gas remaining in a potential halo reservoir, could be interesting for a later work.

In the spiral galaxy subset, we see a mix of behaviours. There is a tendency for present starbursts to show evidence of past/current companion interactions (primarily strong tidal tails, but better number-statistics are necessary to constrain the exact dynamical features). This is consistent with recent results by Zhao et al. (2021), where they find sources with the highest levels of morphological asymmetries lie above the star-forming region. It is also important to note that MS spirals are the most prevalent population in our sample, consistent with recent results for other hard X-ray selected samples (Koutoulidis et al. 2021). What is perhaps most striking is the high fraction of GV-spirals, i.e, with comparatively low SFRs, dominated by smoothly declining old stellar populations. This is consistent with a scenario in which some spiral hosts, predominantly with no signs of dynamical interactions, are evolving passively towards the red sequence. This might point to the relevance of secular processes for the growth and evolution of some spirals galaxies and their SMBHs, particularly in the last 1–4 Gyr. As for the indeterminate sub-sample, we cannot conclude much as we lack the necessary sample numbers to perform a meaningful analysis.

Finally, regarding the possibility of AGN feedback driving the evolution of our sample, we do not find strong evidence in favour of it from a stellar population perspective, with no significant correlation between BH accretion and host SF properties. Given the above discussion, it seems much more likely that either mergers and dynamical interactions or secular processes drive the overall evolution of each galaxy, Naturally, we cannot reject the possibility of AGN having feedback effects, and AGN being a special subset of galaxies with significantly different host properties to those of normal galaxies. In fact, their high SF and merger fractions are significantly different from similar galaxies in stellar mass and redshift range, and so AGN might be triggered in a special subsample of galaxies with a high fraction of these having undergone merger events and other dynamical transformation in the intermediate past.

5.1. *Future steps*

Future work should focus efforts on the following aspects:

- Firstly, the sample subset we base most of our evolutionary conclusions into constitutes about ∼ 6% of the current BASS DR2 sample. This situation significantly hinders our ability to establish more robust results. In particular, we have restricted our analysis to X-SHOOTER data which have few reliable IR-SF measurements.

Despite this, we have analyzed the evolution of our sample as a function of morphology and SFH features. Our results and interpretation would be strengthened by boosting the numbers statistics via the addition of similar spectral resolution spectra from SDSS, Palomar, and other instruments already available for several hundred additional type II AGN in the BASS sample. There are over $\sim$ 800 sources with IR-SFR and stellar mass constraints that could be part of our sample (Secrest et al., in preparation) and be of great help to improve our statistics.

- Secondly, more uniform and robust morphological classification of our sources would help solidify the results. Specifically, including additional archival imaging from other sources would allow a larger fraction of sources to have secondary classifications. Additionally, adding morphologic classifications from a larger pool of collaborators or using more objective techniques or parametrizations (e.g., via GALFIT + residual analyses; GINI coefficients; neural networks) could help to refine the classifications or make them more robust. Finally, we have yet to explore the relationship between current and past SF and the specific merger state the sources are currently in; this merger state could serve as a third morphological classification.
- Finally, we have not analyzed and established a complete and descriptive scenario that explains our optical SF to IR SF differences at high SFR. We attribute most of these differences to the presence of dust and hidden SF in some sources, but these could be correlated to some morphological properties, SFH features, and the state of the gas at the center of the galaxies. A first analysis show that they are spirals, and half of these sources present dynamical features of interactions (either a merger or a close companion). These connections are yet to be explored with better statistics.

6. APPENDIX

6.1. *Definition of SNR and SRR*

Here, we present our definition for SNR and SRR (per pixel-based). Our signal-to-noise ratio definition is the following:

$$SNR = \frac{\text{median(raw spectrum)}}{\text{noise}} \tag{5}$$

where the raw spectrum is the non-masked reduced spectrum before the fitting process, and the noise is an estimation of the noise per pixel based on the square root of the quadratic difference between the non-masked spectrum and a Gaussian-smoothened version of the same array. In the case of the signal-to-residual ratio (SRR):

$$\text{SRR} = \frac{\text{median(spectrum)}}{\sqrt{\text{mean(spectrum-bestfit)}^2}} \tag{6}$$

where the spectrum in this case corresponds to the masked spectrum, ready to be fit. The best fit is our resulting spectral fit, resulting from a linear combination of various templates and weights (3.1).

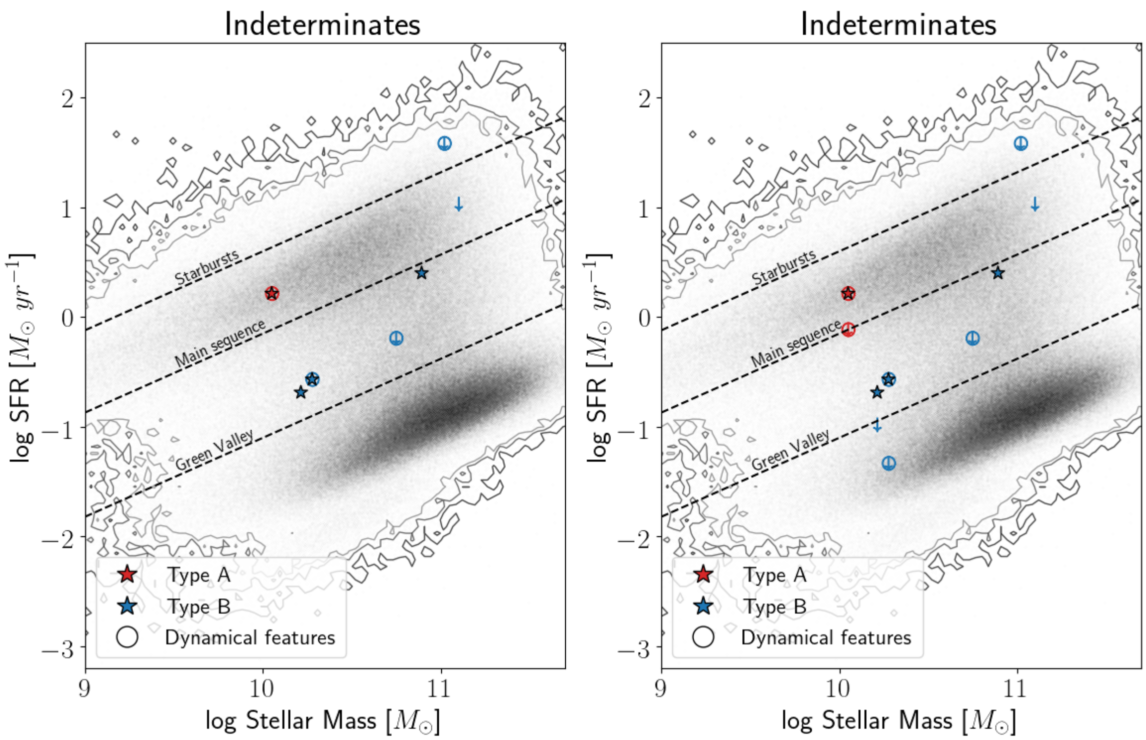

Figure 21: Comparison of SFR vs. stellar mass for our Indeterminate sample (similar to Fig. 16, but with the inclusion of optical limits as per Sec. 4.4). *Red:* Sources with a single stellar population peak at old ages (> 6 Gyr, Type A sources) *Blue*: Every source that does not enter into the former classification (Type B sources). Primarily comprised of sources which show evidence of intermediate or young stellar populations, in addition to an older one. *Dashed lines* denote, from top to bottom, boundaries for the starburst, main sequence, green valley and red sequence SF bands, respectively. *Encircled markers* denote sources that present dynamical interaction features (signs of merger remnant, merger, tails or close companions).

6.2. *Delimiters for each band in the SFR versus stellar mass diagram*

Throughout the thesis, we defined delimiters for each band in such a way that provides helpful binning for our low-sample statistics while being trustful and relatively similar to most previous works. We defined the starburst delimiter as the following linear relationship:

$$\log \mathrm{SFR} = 0.72 \log M - 6.6 \tag{7}$$

(where M correspond to the stellar mass) meaning that all sources above this line will be classified as starburst. In a similar fashion, the upper delimiter line for the main sequence is:

$$\log \mathrm{SFR} = 0.72 \log M - 7.35 \tag{8}$$

Finally, the upper delimiter line for the green valley:

$$\log \mathrm{SFR} = 0.72 \log M - 8.3 \tag{9}$$

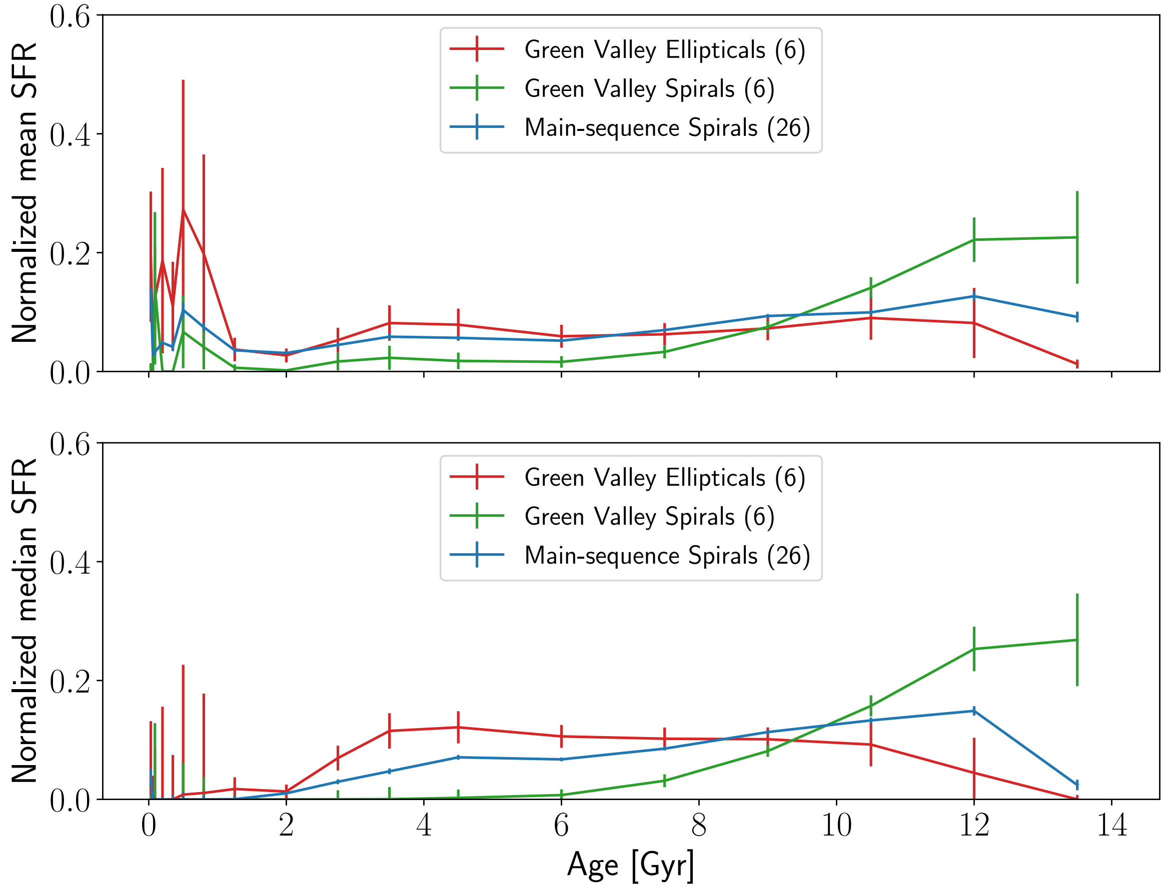

Figure 22: Median star formation histories for the main bands in our analysis (green valley ellipticals, green valley spirals and main sequence spirals).

6.3. *Specific median SFH in the three main bands*

Unfortunately, due our small-sample statistics we are unable to perform a robust comparison between band-specific median SFHs in our sample. However, we still plot our median SFHs for each band in Fig. 22. Broadly speaking, we do find significant differences in their median SFH within out sample: As expected from Fig. 16, GV spirals are dominated by a smoothly decreasing SFH (Type A-like), whereas both the MS Spiral and the GV elliptical band show enhanced star formation in their late-to-intermediate past (Type B-like).

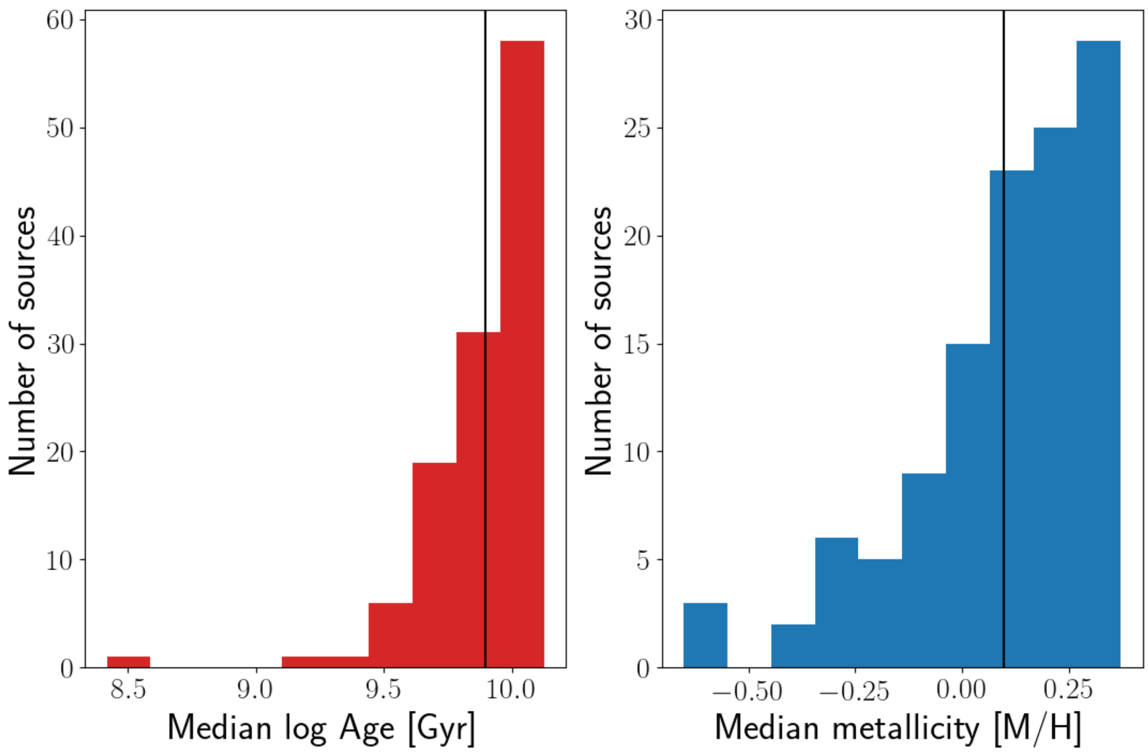

Figure 23: Median mass-weighted ages (left), median mass-weighted metallicities (right) for our X-SHOOTER sample. We plot the mean of each distribution as a vertical black line.

REFERENCES

Aguado, D. S., Ahumada, R., Almeida, A., et al. 2019, ApJS, 240, 23, doi: 10.3847/1538-4365/aaf651

Baldry, I. K., Balogh, M. L., Bower, R., Glazebrook, K., & Nichol, R. C. 2004, in American Institute of Physics Conference Series, Vol. 743, The New Cosmology: Conference on Strings and Cosmology, ed. R. E. Allen, D. V. Nanopoulos, & C. N. Pope, 106–119, doi: 10.1063/1.1848322

Baldwin, J. A., Phillips, M. M., & Terlevich, R. 1981, PASP, 93, 5, doi: 10.1086/130766

Balogh, M. L., Morris, S. L., Yee, H. K. C., Carlberg, R. G., & Ellingson, E. 1999, ApJ, 527, 54, doi: 10.1086/308056

Bell, E. F., McIntosh, D. H., Katz, N., & Weinberg, M. D. 2003, ApJS, 149, 289, doi: 10.1086/378847

Benson, A. J., Bower, R. G., Frenk, C. S., et al. 2003, ApJ, 599, 38, doi: 10.1086/379160

Bower, R. G., Benson, A. J., Malbon, R., et al. 2006, MNRAS, 370, 645, doi: 10.1111/j.1365-2966.2006.10519.x

Bundy, K., Bershady, M. A., Law, D. R., et al. 2015, ApJ, 798, 7, doi: 10.1088/0004-637X/798/1/7

Calzetti, D. 2013, Star Formation Rate Indicators, ed. J. Falcón-Barroso & J. H. Knapen, 419

Calzetti, D., Armus, L., Bohlin, R. C., et al. 2000, ApJ, 533, 682, doi: 10.1086/308692

Cappellari, M. 2017, MNRAS, 466, 798, doi: 10.1093/mnras/stw3020

Cappellari, M., & Emsellem, E. 2004, PASP, 116, 138, doi: 10.1086/381875

Chambers, K. C., Magnier, E. A., Metcalfe, N., et al. 2016, arXiv e-prints, arXiv:1612.05560. https://arxiv.org/abs/1612.05560

Chen, Y.-M., Shi, Y., Wild, V., et al. 2019, MNRAS, 489, 5709, doi: 10.1093/mnras/stz2494

Cid Fernandes, R., Stasińska, G., Mateus, A., & Vale Asari, N. 2011, MNRAS, 413, 1687, doi: 10.1111/j.1365-2966.2011.18244.x

Dey, A., Schlegel, D. J., Lang, D., et al. 2019, AJ, 157, 168, doi: 10.3847/1538-3881/ab089d

Domínguez Sánchez, H., Mignoli, M., Pozzi, F., et al. 2012, MNRAS, 426, 330, doi: 10.1111/j.1365-2966.2012.21710.x

Dubois, Y., Peirani, S., Pichon, C., et al. 2016, MNRAS, 463, 3948, doi: 10.1093/mnras/stw2265

Fabian, A. C. 2012, ARA&A, 50, 455, doi: 10.1146/annurev-astro-081811-125521

Freudling, W., Romaniello, M., Bramich, D. M., et al. 2013, A&A, 559, A96, doi: 10.1051/0004-6361/201322494

Goto, T. 2007, MNRAS, 381, 187, doi: 10.1111/j.1365-2966.2007.12227.x

Gültekin, K., Richstone, D. O., Gebhardt, K., et al. 2009, ApJ, 698, 198, doi: 10.1088/0004-637X/698/1/198

Gunn, J. E., Siegmund, W. A., Mannery, E. J., et al. 2006, AJ, 131, 2332, doi: 10.1086/500975

Hinshaw, G., Larson, D., Komatsu, E., et al. 2013, ApJS, 208, 19, doi: 10.1088/0067-0049/208/2/19

Ichikawa, K., Ricci, C., Ueda, Y., et al. 2019, ApJ, 870, 31, doi: 10.3847/1538-4357/aaef8f

Kauffmann, G., Heckman, T. M., Tremonti, C., et al. 2003, MNRAS, 346, 1055, doi: 10.1111/j.1365-2966.2003.07154.x

Kewley, L. J., Dopita, M. A., Sutherland, R. S., Heisler, C. A., & Trevena, J. 2001, ApJ, 556, 121, doi: 10.1086/321545

Kewley, L. J., Groves, B., Kauffmann, G., & Heckman, T. 2006, MNRAS, 372, 961, doi: 10.1111/j.1365-2966.2006.10859.x

Koss, M., Mushotzky, R., Veilleux, S., et al. 2011, ApJ, 739, 57, doi: 10.1088/0004-637X/739/2/57

Koss, M., Trakhtenbrot, B., Ricci, C., et al. 2017, ApJ, 850, 74, doi: 10.3847/1538-4357/aa8ec9

Koutoulidis, L., Mountrichas, G., Georgantopoulos, I., Pouliasis, E., & Plionis, M. 2021, arXiv e-prints, arXiv:2111.02539. https://arxiv.org/abs/2111.02539

Lang, D. 2014, AJ, 147, 108, doi: 10.1088/0004-6256/147/5/108

Lasker, B. M., Doggett, J., McLean, B., et al. 1996, in Astronomical Society of the Pacific Conference Series, Vol. 101, Astronomical Data Analysis Software and Systems V, ed. G. H. Jacoby & J. Barnes, 88

Madau, P., & Dickinson, M. 2014, ARA&A, 52, 415, doi: 10.1146/annurev-astro-081811-125615

Madau, P., Pozzetti, L., & Dickinson, M. 1998, ApJ, 498, 106, doi: 10.1086/305523

Mushotzky, R. 2004, How are AGN Found?, ed. A. J. Barger, Vol. 308, 53, doi: 10.1007/978-1-4020-2471-9_2

Oh, K., Koss, M., Markwardt, C. B., et al. 2018, ApJS, 235, 4, doi: 10.3847/1538-4365/aaa7fd

Pacifici, C., Kassin, S. A., Weiner, B. J., et al. 2016, ApJ, 832, 79, doi: 10.3847/0004-637X/832/1/79

Peng, Y.-j., Lilly, S. J., Kovač, K., et al. 2010, ApJ, 721, 193, doi: 10.1088/0004-637X/721/1/193

Percival, S. M., Salaris, M., Cassisi, S., & Pietrinferni, A. 2009, ApJ, 690, 427, doi: 10.1088/0004-637X/690/1/427

Rembold, S. B., Shimoia, J. S., Storchi-Bergmann, T., et al. 2017, MNRAS, 472, 4382, doi: 10.1093/mnras/stx2264

Ricci, C., Trakhtenbrot, B., Koss, M. J., et al. 2017, ApJS, 233, 17, doi: 10.3847/1538-4365/aa96ad

Salpeter, E. E. 1955, ApJ, 121, 161, doi: 10.1086/145971

Sánchez, S. F., Avila-Reese, V., Hernandez-Toledo, H., et al. 2018, RMxAA, 54, 217. https://arxiv.org/abs/1709.05438

Schawinski, K., Virani, S., Simmons, B., et al. 2009, ApJL, 692, L19, doi: 10.1088/0004-637X/692/1/L19

Schawinski, K., Urry, C. M., Simmons, B. D., et al. 2014, MNRAS, 440, 889, doi: 10.1093/mnras/stu327

Shimizu, T. T., Mushotzky, R. F., Meléndez, M., et al. 2017, MNRAS, 466, 3161, doi: 10.1093/mnras/stw3268

Strateva, I., Ivezić, Ž., Knapp, G. R., et al. 2001, AJ, 122, 1861, doi: 10.1086/323301

Worthey, G. 1994, ApJS, 95, 107, doi: 10.1086/192096

Worthey, G., & Ottaviani, D. L. 1997, ApJS, 111, 377, doi: 10.1086/313021

Wylezalek, D., Flores, A. M., Zakamska, N. L., Greene, J. E., & Riffel, R. A. 2020, MNRAS, 492, 4680, doi: 10.1093/mnras/staa062

York, D. G., Adelman, J., Anderson, John E., J., et al. 2000, AJ, 120, 1579, doi: 10.1086/301513

Zhao, Y., Li, Y. A., Shangguan, J., Zhuang, M.-Y., & Ho, L. C. 2021, arXiv e-prints, arXiv:2111.03558. https://arxiv.org/abs/2111.03558

Zou, F., Yang, G., Brandt, W. N., & Xue, Y. 2019, ApJ, 878, 11, doi: 10.3847/1538-4357/ab1eb1